Nonhydrostatic, Three-Dimensional Perturbations to Balanced, Hurricane-Like Vortices. Part II: Symmetric Response and Nonlinear Simulations

DAVID S. NOLAN

Rosenstiel School of Marine and Atmospheric Science, University of Miami, Miami, Florida

LEWIS D. GRASSO

Cooperative Institute for Research in the Atmosphere, Fort Collins, Colorado

(Manuscript received 28 November 2002, in final form 29 April 2003)

ABSTRACT

This paper is the second part of a study on the dynamics of nonhydrostatic perturbations to dry, balanced, atmospheric vortices modeled after tropical cyclones. In Part I, the stability and evolution of asymmetric perturbations were presented. This part is devoted to the stability and evolution of symmetric perturbations—particularly those that are induced by the wave–mean flow interactions of asymmetric perturbations with the symmetric basic-state vortex.

The linear model shows that the vortices considered in Part I are stable to symmetric perturbations. Furthermore, the model can be used to derive the steady, symmetric response to stationary symmetric forcing, similar to the results from quasi-balanced dynamics as originally presented by Eliassen. The secondary circulations that develop act to oppose the effects of the forcing, but also to warm the core and intensify the vortex. The model is also used to simulate the response to impulsive symmetric forcings, that is, symmetric perturbations. Much like the asymmetries considered in Part I, symmetric perturbations go through two kinds of adjustment: a fast adjustment that generates gravity waves, and then a slow adjustment leading to a final state that represents a net change in both the wind and mass fields of the symmetric vortex.

The nonhydrostatic, unsteady, symmetric response of the tropical-storm-like vortex to the evolving asymmetries from Part I is presented. In contrast with results from previous studies with initially two-dimensional or balanced asymmetric vorticity perturbations, asymmetric temperature perturbations are found to have a negative effect on overall intensity. These changes are about two orders of magnitude smaller than those caused by symmetric perturbations of equal amplitude. The asymmetric/symmetric adjustment process for purely asymmetric temperature perturbations are also simulated with a fully nonlinear, compressible model. Excellent agreement is found between the linear, nonhydrostatic and the nonlinear, compressible models. The vortex intensification caused by a localized, impulsive thermal perturbation can be accurately estimated from the projection of this perturbation onto the purely symmetric motions.

1. Introduction

While mature hurricanes often exhibit remarkably axisymmetric structures, developing tropical cyclones are generally quite asymmetric, particularly with regard to their convection and precipitation fields. Nonetheless, it is the heating associated with this convection and precipitation that maintains, or may even intensify, the larger vortex, even though the convection may be highly localized in areas not close to the vortex center. The example of Tropical Storm Edouard (2002) is shown in Fig. 1. During this period, Edouard was in a hostile environment with substantial northwesterly shear and entrainment of dry air from the mainland United States. As a result, the convection was intermittent and well to the east of the storm center. Nonetheless, the maximum wind speed as estimated by the National Hurricane Center increased from 35 to 50 kt, and the minimum surface pressure fell from 1005 to 1002 hPa. Later in its lifetime, Edouard maintained itself in a hostile environment for several days solely from the support of sporadic bursts of convection south and east (downshear) of the center. The predominance of deep convection on the downshear side of vertically sheared storms (and its absence on the upshear side) has been extensively documented (Reasor et al. 2000; Frank and Ritchie 2001; Black et al. 2002; Corbosiero and Molinari 2002).

In a series of recent investigations, it has been shown that asymmetric vorticity perturbations introduced into the vicinity of a stable vortex will ultimately lead to the intensification of that vortex, in terms of its maximum wind speeds or total kinetic energy (Carr and Williams

Corresponding author address: Prof. David S. Nolan, RSMAS/MPO, University of Miami, 4600 Rickenbacker Causeway, Miami, FL 33149.
E-mail: dnolan@rsmas.miami.edu

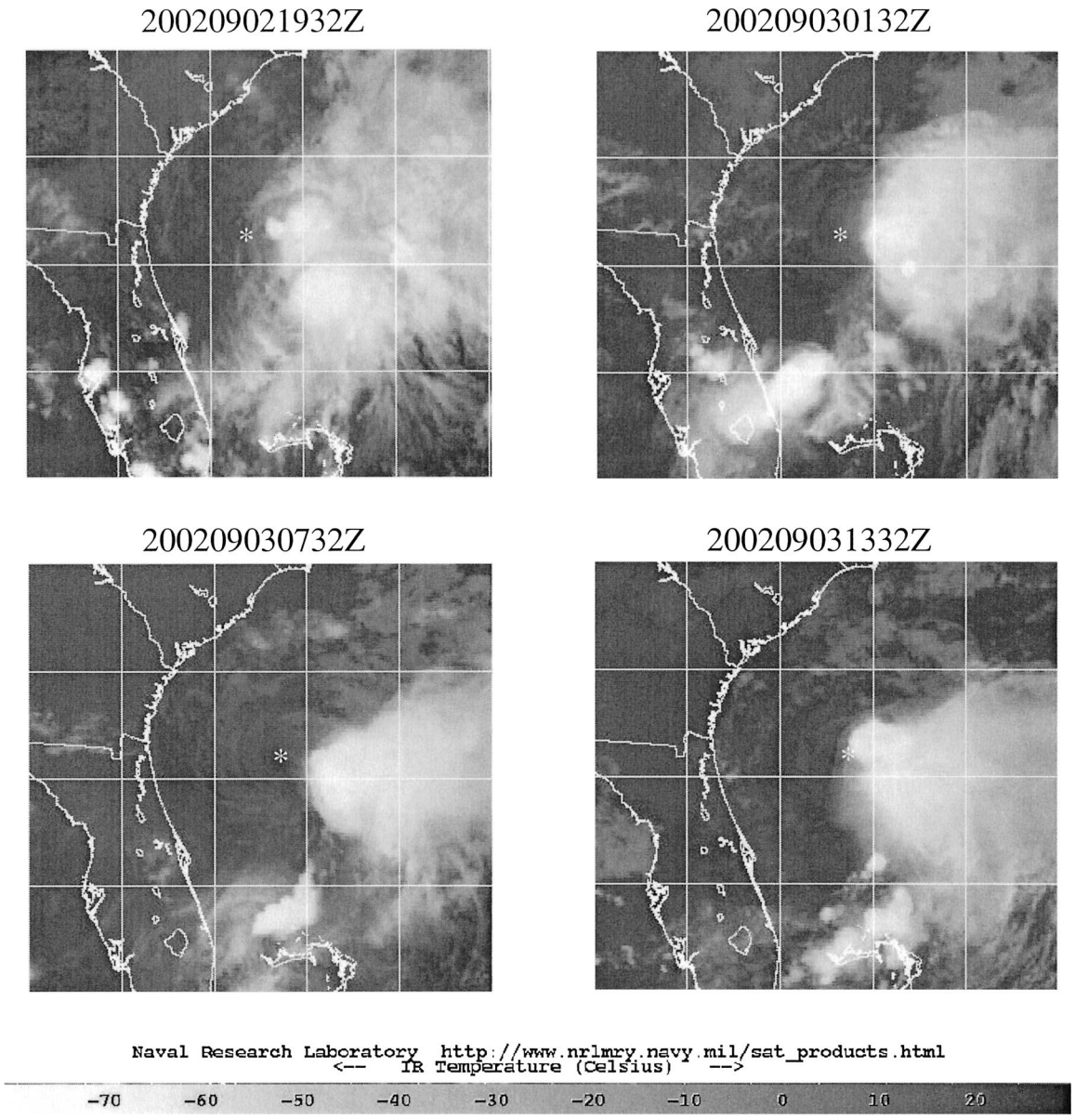

FIG. 1. *Geostationary Operational Environmental Satellite-8* (*GOES-8*) infrared images of Tropical Storm Edouard in 2002. Images cover from 26° to 32°N latitude, 74° to 84°W longitude; lines mark 2° increments. Images were obtained from the Naval Research Laboratory. Approximate storm center locations are indicated by asterisks.

1989; Smith and Montgomery 1995; Montgomery and Kallenbach 1997; Montgomery and Enagonio 1998; Nolan and Farrell 1999a,b; Möller and Montgomery 1999, 2000; Shapiro 2000; Enagonio and Montgomery 2001). As these vorticity perturbations are sheared by the differential wind speeds of the larger vortex, they induce eddy momentum fluxes, which transport angular momentum inward, increasing the kinetic energy of the symmetric flow. In agreement with the conservation of energy, the amplitudes of the asymmetries decay rapidly. This process is generally called ''axisymmetrization'' (see, e.g., Melander et al. 1987).

In (Nolan and Montgomery 2002b, hereafter Part I), a numerical method was presented that solved for the linearized, nonhydrostatic evolution of asymmetric perturbations to an axisymmetric vortex with arbitrary radial and vertical structure. This linear model was used to determine the stability and linearized evolution of asymmetric perturbations to balanced vortices whose wind fields were modeled after tropical cyclones. In particular, it was shown that an intense, hurricane-like vortex could support exponentially growing modes with *e*-folding times on the order of a few hours.

The majority of the aforementioned studies on axisymmetrization considered the evolution of initially two-dimensional or balanced vorticity asymmetries,

generally presumed to be the end result of an adjustment to convection displaced from the vortex center. In Part I, asymmetric temperature perturbations, introduced instantaneously, were studied as a complement and contrast to previous work. These unbalanced thermal asymmetries went through a two-stage adjustment process. The first stage involved a rapid adjustment to hydrostatic balance with concomitant gravity wave radiation. This left behind quasi-balanced vorticity perturbations, which, in the second stage of adjustment, were axisymmetrized by the shear of the background flow. While an analysis of the eddy heat and momentum fluxes associated with these axisymmetrizing perturbations suggested that intensification of the symmetric vortex was possible, a more complete analysis was left for this study.

This more complete analysis recognizes that, for a balanced vortex, changes to the symmetric wind or mass fields result in an additional adjustment process, whereby the symmetric vortex adjusts to regain both hydrostatic and gradient wind balance. Under the assumption of a ''balanced'' response, Eliassen (1951) showed how symmetric circulations are generated by sources of heat or momentum in a symmetric vortex. Using the same methodology as described for asymmetric motions in Part I, we develop in section 2 a linear model that solves for the fully nonhydrostatic (and nonbalanced) response of a symmetric vortex to symmetric forcings. Before addressing the symmetric response to asymmetric dynamics, the linear model is first used in section 3 to diagnose the unsteady, nonhydrostatic response of the vortex to symmetric sources of heat and momentum; these results help us to understand the response to asymmetric forcing. In section 4, symmetric tendencies caused by the heat and momentum fluxes of the asymmetric perturbations considered in Part I are used as time-dependent forcings for the symmetric motions, thus determining the full response of the symmetric vortex to nonhydrostatic, asymmetric perturbations. A number of additional simulations are performed to show how these results depend on the wavenumber, the location of the forcing, and the strength of the diffusion. Results from this linear model are compared to matched simulations in a fully compressible, nonlinear model in section 5. Conclusions are presented in section 6.

2. The symmetric hurricane equations

The equations for perturbations to axisymmetric, hurricane-like or tornado-like vortices were derived in Part I [Eqs. (2.1)–(2.13)]. Setting the azimuthal wavenumber n equal to zero generates the *symmetric tornado–hurricane equations* (STHE):

$$\frac{\partial u_0}{\partial t} + \overline{u}\frac{\partial u_0}{\partial r} + \overline{w}\frac{\partial u_0}{\partial z} + u_0\frac{\partial \overline{u}}{\partial r} + w_0\frac{\partial \overline{u}}{\partial z} - (2\overline{\Omega} + f)v_0 = -\frac{1}{\overline{\rho}}\frac{\partial p_0}{\partial r} + F_u + E_u, \tag{2.1}$$

$$\frac{\partial v_0}{\partial t} + \overline{u}\frac{\partial v_0}{\partial r} + \overline{w}\frac{\partial v_0}{\partial z} + w_0\frac{\partial \overline{v}}{\partial z} + \left(\frac{\partial \overline{v}}{\partial r} + \overline{\Omega} + f\right)u_0 + \frac{\overline{u}}{r}v_0 = F_v + E_v, \tag{2.2}$$

$$\frac{\partial w_0}{\partial t} + \overline{u}\frac{\partial w_0}{\partial r} + \overline{w}\frac{\partial w_0}{\partial z} + u_0\frac{\partial \overline{w}}{\partial r} + w_0\frac{\partial \overline{w}}{\partial z} = -\frac{1}{\overline{\rho}}\frac{\partial p_0}{\partial z} + g\frac{\theta_0}{\overline{\theta}} + F_w + E_w, \tag{2.3}$$

$$\frac{\partial \theta_0}{\partial t} + \overline{u}\frac{\partial \theta_0}{\partial r} + \overline{w}\frac{\partial \theta_0}{\partial z} + u_0\frac{\partial \overline{\theta}}{\partial r} + w_0\frac{\partial \overline{\theta}}{\partial z} = F_\theta + E_\theta, \tag{2.4}$$

$$\frac{1}{r\overline{\rho}}\frac{\partial}{\partial r}(r\overline{\rho}u_0) + \frac{1}{\overline{\rho}}\frac{\partial}{\partial z}(\overline{\rho}w_0) = 0, \tag{2.5}$$

where u, v, w, r, and z have their usual meanings; θ is the potential temperature; and $\overline{\rho} = \overline{\rho}(r, z)$ is the anelastic density, which does not change in time. The F parameters are frictional terms, and to each of the four conservation equations, we have added to the rhs a source term representing the tendencies due to the divergences of eddy fluxes caused by asymmetric perturbations [E_u, E_v, . . . cf. (4.2)–(4.6) in Part I]. Terms representing the basic-state meridional circulation have also been included, although they will not be considered in the present work.

In the asymmetric equations, v_n and p_n appear undifferentiated in the incompressibility condition and the azimuthal momentum equations, respectively. These variables could then be eliminated from the other equations by direct substitution, thus reducing the number of equations from five to three. This is not possible with the symmetric equations, as these undifferentiated terms are not present where $n = 0$. Rather, the number of variables may be reduced through the use of a streamfunction, for example,[1]

$$u_0 = -\frac{1}{\overline{\rho}r}\frac{\partial \psi_0}{\partial z}, \qquad w_0 = \frac{1}{\overline{\rho}r}\frac{\partial \psi_0}{\partial r}. \tag{2.6}$$

The pressure is eliminated by first multiplying (2.1) and (2.3) by $\overline{\rho}$, then subtracting $\partial/\partial r$ of (2.3) from $\partial/\partial z$ of (2.1). The result is a streamfunction-vorticity formulation of the symmetric perturbation equations, coupled with equations for v_0 and θ_0. These are shown in appendix A.

In Part I, standard laminar diffusion with a constant eddy viscosity was added to the equations to suppress computational instabilities, and Newtonian damping regions (i.e., ''sponges'') were used near the upper and outer boundaries to suppress the reflection of gravity waves. For consistency, these are both used for the sym-

[1] Alternatively, one may use $u = -(1/\overline{\rho})[\partial(\overline{\rho}\psi)/\partial z]$ and $w = [1/(\rho r)][\partial(\rho r\psi)/\partial r]$, and reverse the signs in either case.

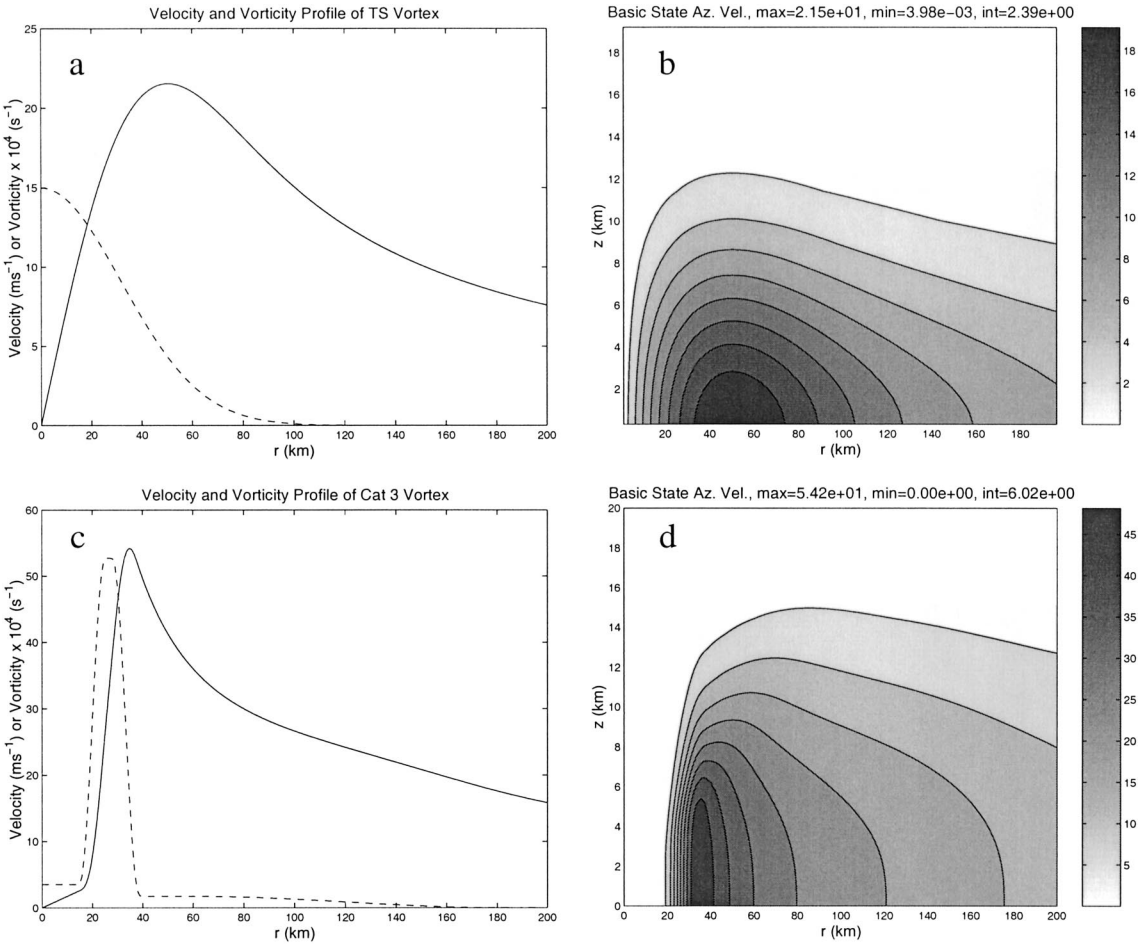

FIG. 2. Radial and vertical profiles of the basic-state vortices used for this study: (a) $v(r)$ and $\zeta(r)$ for the tropical-storm-like vortex; (b) $v(r, z)$ for the tropical-storm-like vortex; (c) $v(r)$ and $\zeta(r)$ for the category 3 vortex; (d) $v(r, z)$ for the category 3 vortex.

metric analyses here [(2.14)–(2.18) in Part I], with an eddy viscosity $\nu = 40\ \mathrm{m^2\ s^{-1}}$ except where noted. Free-slip, solid-wall boundary conditions were enforced on all sides, as described in appendix B.

Unlike in Part I, we will consider the *forced* evolution of the perturbations. The linear dynamical system that describes the flow evolution must be augmented to include the forcing; that is,

$$\frac{d}{dt}(\mathbf{Bx}) = \mathbf{Ax} + \mathbf{h}, \tag{2.7}$$

where $\mathbf{x}$ is a state vector containing the elements of ψ_0, v_0, and θ_0; $\mathbf{h}$ is a vector containing the tendencies for each of these elements (E_u, E_v, etc.); and $\mathbf{A}$ and $\mathbf{B}$ are matrix representations of second-order approximations to the differential operators outlined in appendix A. Time evolution is solved by integrating

$$\frac{d\mathbf{x}}{dt} = \mathbf{B}^{-1}\mathbf{Ax} + \mathbf{B}^{-1}\mathbf{h}, \tag{2.8}$$

with a fourth-order Runge–Kutta scheme. A time step of 30 s was used for all simulations.

3. Response to idealized, symmetric forcing

a. The basic-state vortices and their stability

The basic state vortices constructed in Part I (section 3) were designed to have their potential vorticity $\overline{q} > 0$ everywhere, such that the vortices were not susceptible to symmetric or inertial instabilities. Our numerical analysis confirms that neither the category 3, category 1, or tropical-storm-like vortices support exponentially growing symmetric modes. Calculations[2] found that all the eigenvalues of the time evolution matrix $\mathbf{T} = \mathbf{B}^{-1}\mathbf{A}$ had negative real parts for values of eddy viscosity $\nu \geq 5\ \mathrm{m^2\ s^{-1}}$. For reference, radial and vertical profiles of vorticity and velocity for the tropical-storm and category 3 vortices are shown in Fig. 2. For all results here and in Part I, the Coriolis parameter $f = 5.0 \times 10^{-5}\ \mathrm{s^{-1}}$ (regretfully, this was not stated in Part I).

[2] All calculations were performed with Matlab 6.0 or recent upgrades.

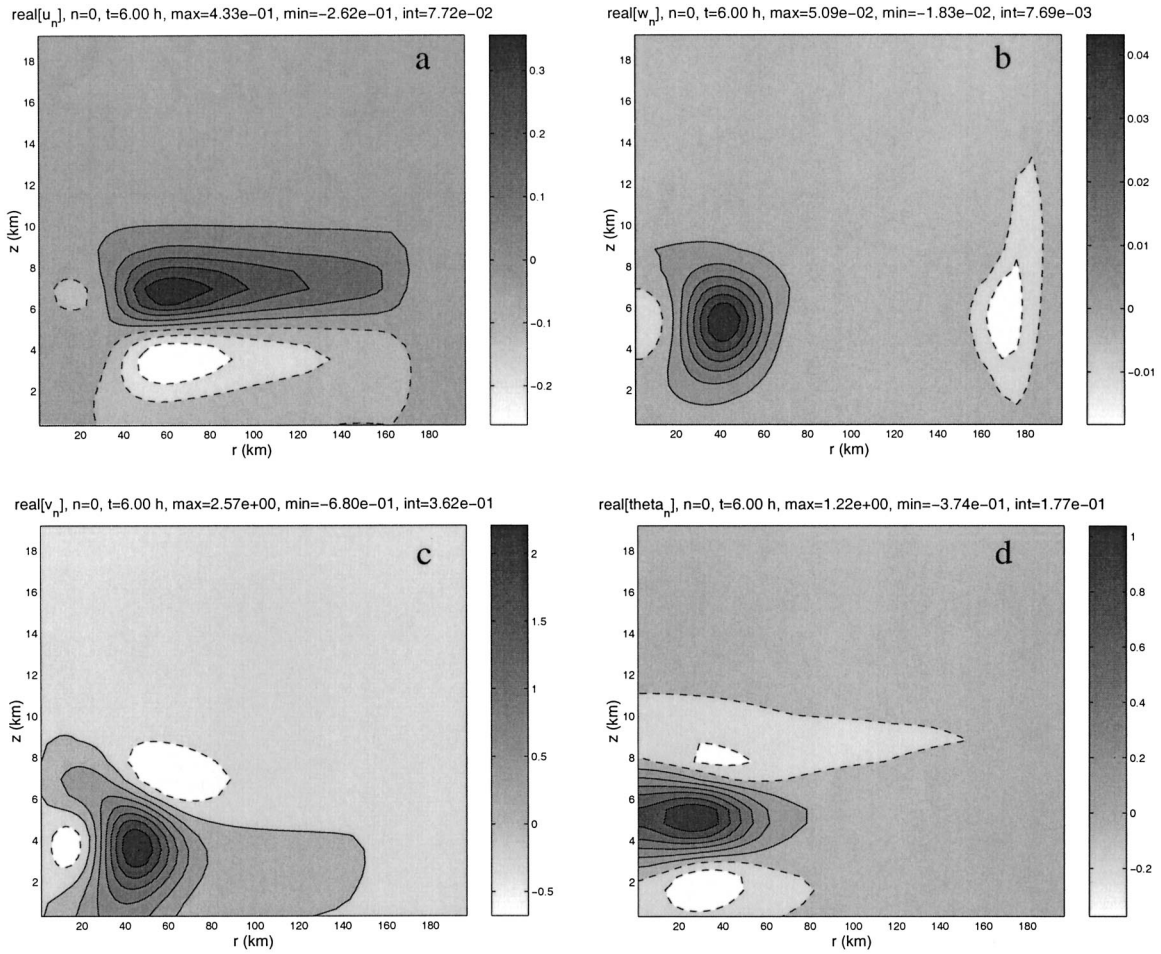

FIG. 3. Steady, symmetric response at $t = 6$ h of the tropical-storm-like vortex to a Gaussian-shaped heat source at $r_b = 40$ km, $z_b = 5$ km: (a) radial velocity; (b) vertical velocity; (c) azimuthal velocity; (d) potential temperature. Units are mks.

b. Steady forcing

Under the assumption that the vortex must remain in gradient wind balance, Eliassen (1951) showed how the secondary circulation, which maintains this balance, could be computed directly from arbitrary thermal or momentum forcings with a Green's function method. While Eliassen considered only vortices with simple vertical and horizontal structures, Shapiro and Willoughby (1982) numerically extended Eliassen's formulation to balanced vortices of arbitrary structure, much like those considered in Part I. Most significantly, they showed how the symmetric response can depend quite strongly on the larger properties of the basic-state vortex. For example, if the vorticity profile drops off rapidly with radius from the inner core of the storm (typical for tropical cyclones, and in contrast to the simple vortices Eliassen considered), the inertial stability is greatly decreased in the outer region and the circulation can extend to great distances in the horizontal (cf. Shapiro and Willoughby 1982, Fig. 9).

We can also consider a balanced response with our nonhydrostatic formulation by assuming that such a response is equivalent to the secondary circulation that would develop from steady forcing. A quasi-steady state is achieved when the local changes induced by the secondary circulation balance the effects of the forcing, which is essentially the assumption behind Eliassen's (1951) derivation. To demonstrate this steady, balanced response, we evolve symmetric perturbations to the tropical storm vortex, forced by a Gaussian-shaped bubble of thermal tendency; that is,

$$h_\theta = \dot{\theta}_0 \exp\left[-\left(\frac{r - r_b}{\sigma_r}\right)^2 - \left(\frac{z - z_b}{\sigma_z}\right)^2\right], \quad (3.1)$$

where $r_b = 40$ km is the radial location, $z_b = 5$ km is the altitude, $\sigma_r = 20$ km is the radial half-width, $\sigma_z = 2$ km is the vertical half-width, and $\dot{\theta}_0 = 1$ K h^{-1} is the heating rate amplitude. After a period of unsteady dynamics lasting less than an hour, a secondary circulation in u_0 and w_0 develops, which becomes virtually constant in time. This circulation at $t = 6$ h is shown in Fig. 3. Also shown are the v_0 and θ_0 fields that have developed

TABLE 1. Symmetric simulations of the tropical storm vortex with symmetric forcing, where $z_b = 5$ km throughout.

Forcing type	r_b (km)	Magnitude	Surface-center Δp at $t = 6$ h (hPa)	Surface Δv at RMW at $t = 6$ h (m s^{-1})
Steady thermal	40	$\dot{\theta} = 1$ K h^{-1}	-0.54	0.81
	80	$\dot{\theta} = 1$ K h^{-1}	-0.17	0.19
Steady velocity	40	$\dot{v} = 1$ m s^{-1} h^{-1}	-0.39	0.45
	80	$\dot{v} = 1$ m s^{-1} h^{-1}	-0.24	0.32
Impulsive thermal	40	$\theta = 1$ K	-9.1×10^{-2}	0.16
	80	$\theta = 1$ K	-2.7×10^{-2}	0.032
Impulsive velocity	40	$v = 1$ m s^{-1}	-7.2×10^{-2}	0.095
	80	$v = 1$ m s^{-1}	-4.3×10^{-2}	0.054
Symmetric projection	40	$\theta = 0.14$ K	-1.4×10^{-2}	0.023
of displaced 1-K	60	$\theta = 0.09$ K	-0.51×10^{-2}	0.010
bubble	80	$\theta = 0.07$ K	-0.20×10^{-2}	0.0025

in response. While the vertical motion field acts to balance the thermal forcing via adiabatic cooling, the induced secondary circulation causes downward motion and warming along the axis, and increases the wind speeds down to the surface. This result is very similar to those presented by Shapiro and Willoughby (1982, Fig. 9) for point sources of heat. The circulation is closed off near the outer boundary. While the secondary circulation remains constant, the v_0 and θ_0 fields (which represent changes of the basic-state vortex) increase linearly with time. The increase in v_0 after 6 h is 2.57 m s^{-1} aloft and 0.81 m s^{-1} at the surface at the radius of maximum winds (RMW), indicating that this Gaussian bubble of 1 K h^{-1} heating causes an increase of 0.15 m s^{-1} h^{-1} at the RMW. For forcing at $r_b = 80$ km, the overall response was similar but much smaller in amplitude; the tendency at the surface at the RMW was only 0.03 m s^{-1} h^{-1} (see Table 1).

Alternatively, one expects that an exact, steady state is reached in (2.8) when

$$\mathbf{x} = -\mathbf{A}^{-1}\mathbf{h}. \tag{3.2}$$

However, numerical simulations showed that this state is achieved only after several days of steady forcing. While the steady-state u_0 and w_0 fields from (3.2) were very similar to those above, their associated tendencies on the v_0 and w_0 fields, and these fields themselves, were highly dependent on the value of the viscosity, indicating that the $t \to \infty$ limit is achieved only when the v_0 and w_0 fields become so large that the diffusive tendencies are substantial. Thus, it is the short-time, quasi-steady response shown above that is physically meaningful and representative of Eliassen's (1951) solutions.

We repeated these calculations for a region of azimuthal velocity forcing h_v, with the same Gaussian structure as (3.1), and a maximum tendency $\dot{v}_0 = 1$ m s^{-1} h^{-1}. The results are shown in Fig. 4 and Table 1, and are again similar to those found by Shapiro and Willoughby (1982, Fig. 12). The tendency at the surface RMW is 0.075 m s^{-1} h^{-1}; for $r_b = 80$ km, it is 0.063 m s^{-1} h^{-1}. Note the reduction in intensification for forcing at larger radii is not as drastic for velocity forcing.

c. Impulsive forcing

The opposite extreme from steady forcing is impulsive forcing. As an approximation to intense forcing over a short period of time, we consider the evolution of symmetric perturbations to the azimuthal wind and potential temperature fields. A warm bubble with the same structure as in (3.1), but with a 1-K maximum amplitude, was used as an initial condition and allowed to evolve without forcing. During the first hour, the dynamics are dominated by a direct response to the warm bubble, with upward motion in its vicinity and subsidence on either side (Figs. 5a and 5b). These motions generate axisymmetric gravity waves; the phase speeds of these waves decrease with increasing vertical wavenumber. Thus, while the gravest waves propagate out of the domain quickly, the higher-wavenumber gravity waves eventually organize into an outward-traveling packet that is still visible emanating out of the vortex after 4–6 h (Fig. 5c). At the same time, we can see the appearance of a change in the azimuthal velocity field (Fig. 5d). After 8 h, the oscillations associated with the gravity waves have subsided (not shown), and the symmetric perturbation shows a stronger wind field (especially aloft) and a warmer core at midlevels (Figs. 5e and 5f).

We also performed simulations for an identical symmetric perturbation to the azimuthal velocity field. The evolution is shown in Fig. 6, with a similar packet of symmetric gravity waves radiating outward, a net increase to the wind field, and a warmer core at midlevels. It is interesting to note that for both types of forcing, the net change caused by an impulsive forcing has a nearly identical structure to the tendencies caused by steady forcing (cf. Fig. 5e to Fig. 3c, and Fig. 6e to Fig. 4c). Indeed, under linear dynamics, the equilibrated response to a time-integrated forcing should be equal to an equivalent sum of smaller, shorter forcings.

The variable that most easily identifies changes in overall tropical cyclone intensity is the surface pressure at the center of the storm. Figure 7 shows the time evolution of the central surface pressure perturbations the two cases above, and also for temperature and ve-

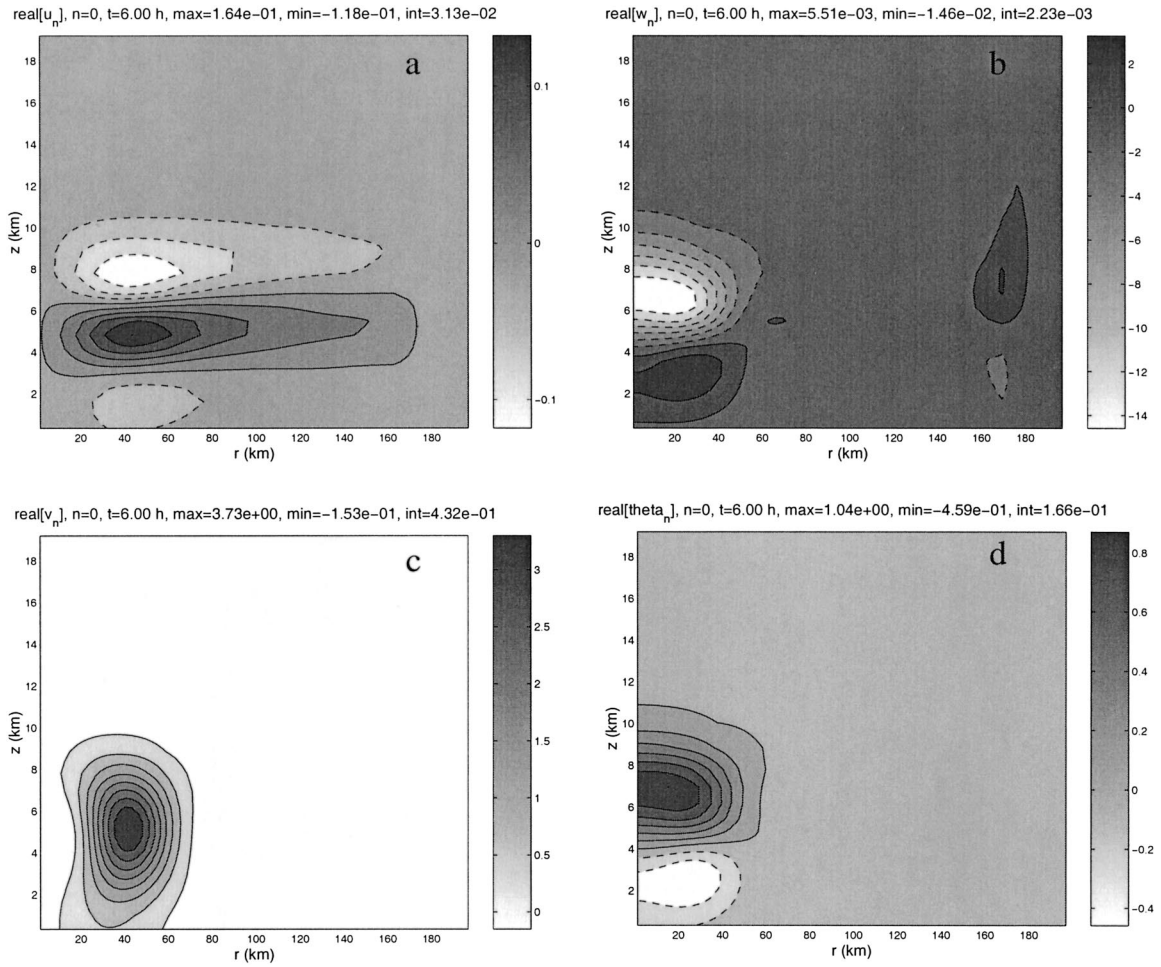

FIG. 4. As in Fig. 3, but for the response to a Gaussian-shaped region of azimuthal velocity forcing at $r_b = 40$ km, $z_b = 5$ km.

locity perturbations at $r_b = 80$ km. For the symmetric thermal bubbles, there are significant oscillations before the pressure settles[3] to perturbations of -0.091 and -0.027 hPa for the $r_b = 40$- and 80-km bubbles, respectively. The pressure drops caused by the velocity bubbles are comparable, -0.072 and -0.043 hPa (see Table 1). Also shown in Fig. 7 are the final ($t = 8$ h) changes to the surface winds for each case; the changes in surface wind are positive everywhere, and peaked below the sources of heat or momentum.

In Part I, hydrostatic pressure fields were also computed and compared to the anelastic pressure fields. For symmetric adjustment, the hydrostatic surface pressures followed the anelastic pressures closely, but during the early adjustment period the hydrostatic oscillations were approximately twice as large (not shown). This suggests that the vertical and radial motions in a hydrostatic model would be too large, as has been shown for hydrostatic models with grid spacing less than 8 km (Weisman et al. 1997).

4. Response to forcing from asymmetric dynamics

The balanced and dynamic responses of the symmetric vortex to symmetric forcings serve as reference for understanding the response to forcings caused by asymmetric perturbations. In Part I, two types of asymmetries were studied: those generated by instabilities, and those generated as the reponse to an asymmetric temperature perturbation. We examine each of these in turn.

a. Exponentially growing modes

We consider the case of the most unstable mode for the category 3 hurricane-like vortex analyzed in Part I, which occurs for azimuthal wavenumber $n = 3$ and has

[3] To be clear, diffusion in the model eventually relaxes all the perturbations back to zero. However, in most of our simulations, the symmetric perturbations reach a quasi-steady state after the interesting dynamics have subsided, which then decays slowly due to frictional effects. This quasi-steady state is referred to as a ''final'' state or net change to the symmetric vortex.

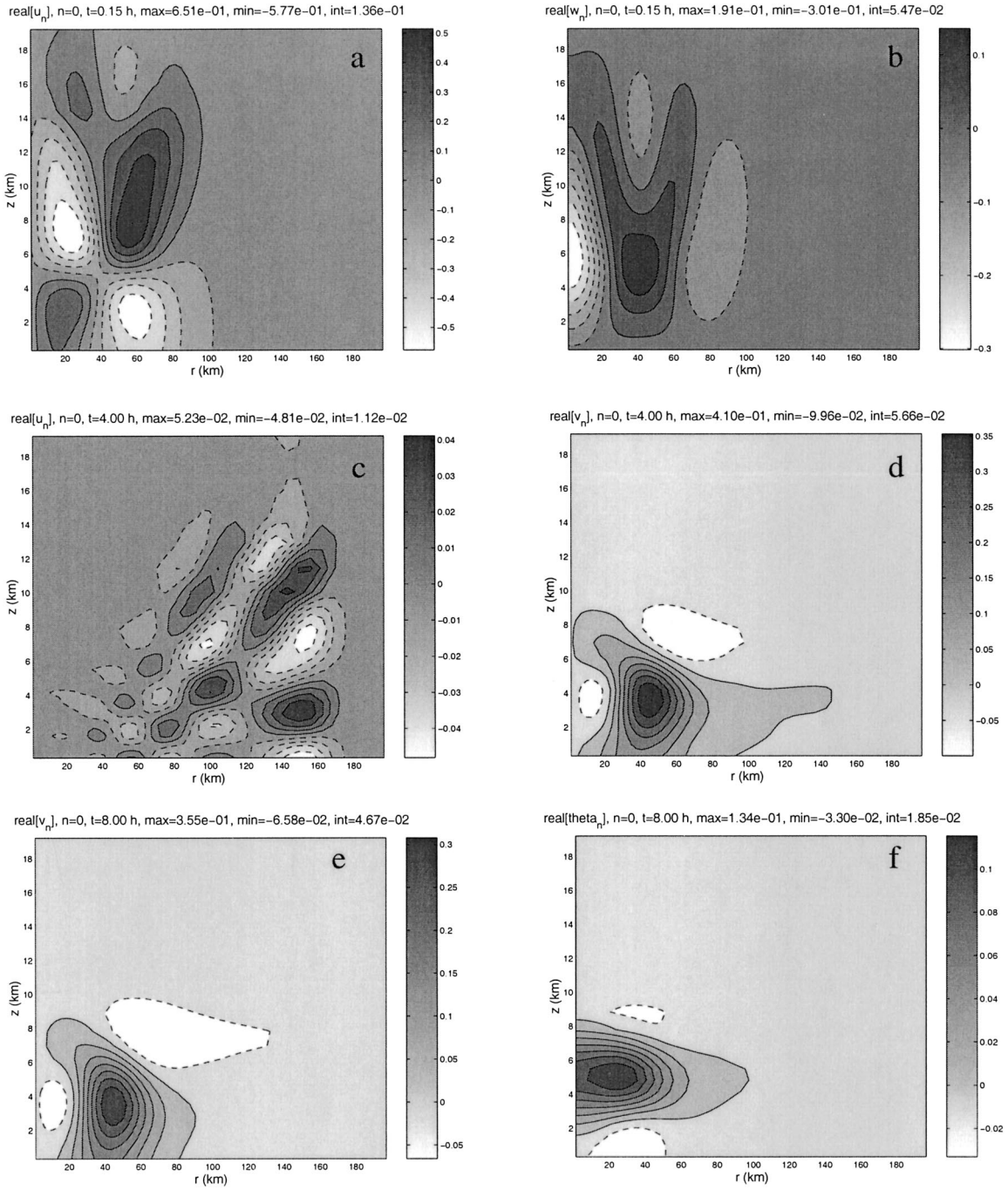

FIG. 5. Evolution of the symmetric response to a Gaussian-shaped symmetric warm bubble at $r_b = 40$ km, $z_b = 5$ km: (a) radial velocity at $t = 10$ min; (b) vertical velocity at $t = 10$ min; (c) radial velocity at $t = 4$ h; (d) azimuthal velocity at $t = 4$ h; (e) azimuthal velocity at $t = 8$ h; (f) potential temperature at $t = 8$ h.

an *e*-folding time of 1.34 h. The eddy-flux-induced tendencies have a fixed structure that grow exponentially in time with the unstable mode. The tendencies for u_0, v_0, w_0, and θ_0 are shown in Figs. 7 and 8 of Part I. The amplitudes of these tendencies were recomputed to be initially those of a mode with maximum radial windspeeds of 0.01 m s^{-1}; this value is chosen simply as a small-amplitude initial condition. The tendencies for $t > 0$ were computed based on the exponential growth rate of the most unstable mode. (Since eddy flux terms scale like $u'v'$, tendencies grow at twice the exponential rate of the mode.) These tendencies were used to force the symmetric equations for 12 h. During 3-min intervals of the symmetric evolution, the means of the ten-

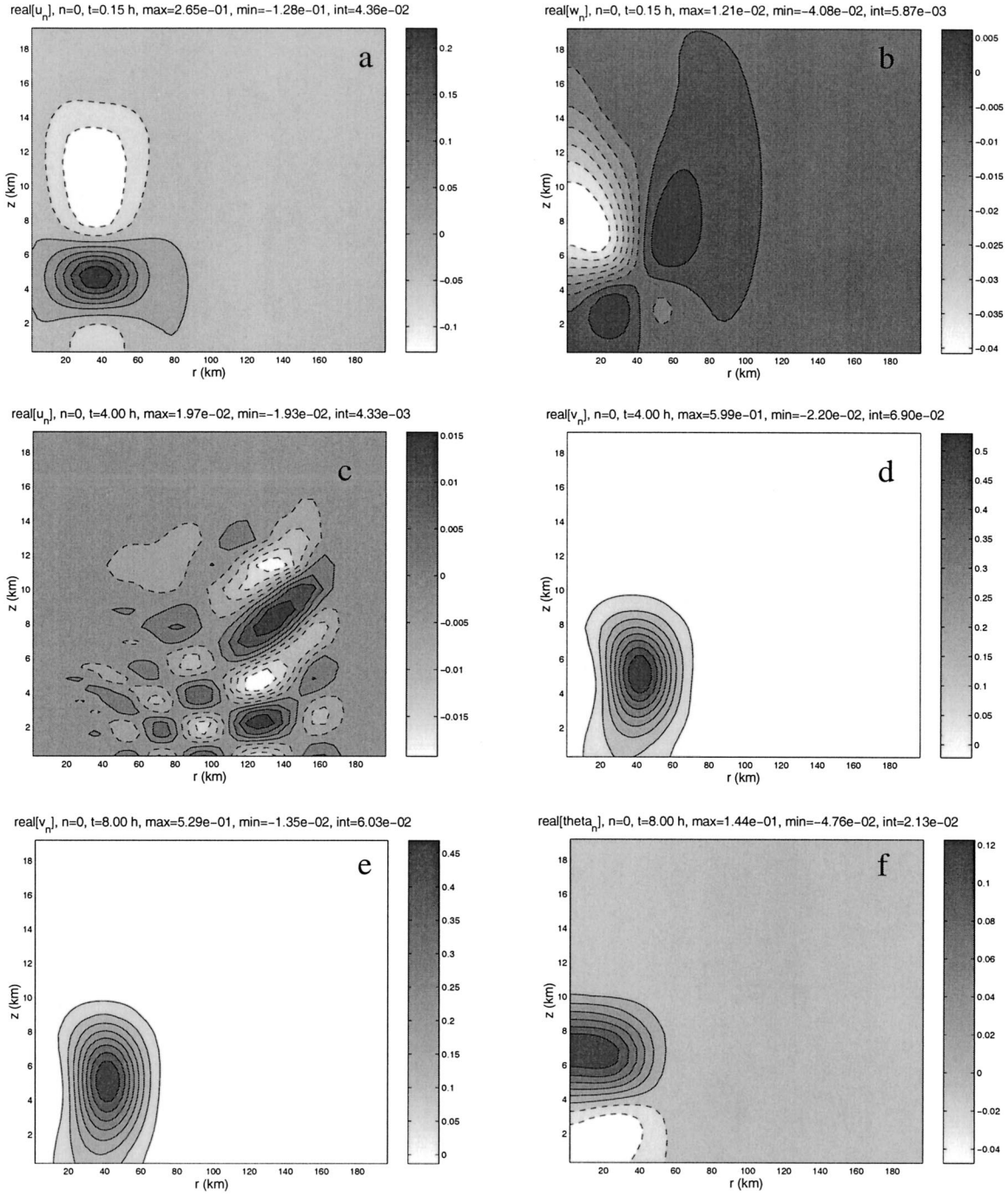

FIG. 6. As in Fig. 5, but for a 1 m s^{-1} Gaussian-shaped velocity perturbation.

dencies at each end of the interval was used to compute **h** (i.e., trapezoidal integration); this method was used in all subsequent calculations with time-dependent tendencies.

While the amplitude of the symmetric response grew exponentially with the mode, its structure was nearly constant after the first hour of simulation time. The symmetric response at $t = 8$ h is shown in Fig. 7. The azimuthal wind and potential temperature fields are very much like what one might expect from simply considering the forcing; the velocity field is enhanced inside the radius of maximum winds ($r = 34.5$ km for the category 3 vortex), where there are also increased temperatures and falling surface pressures (pressures not shown). Away from the modal forcing, there is evidently a weaker secondary circulation that penetrates inward

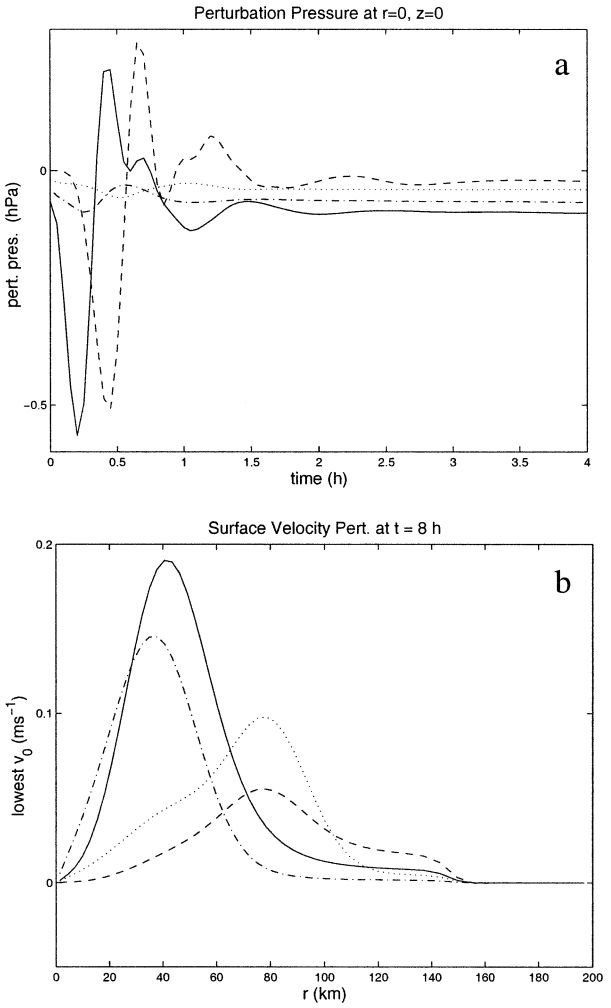

FIG. 7. Central surface pressure perturbation as a function of (a) time and (b) surface velocity change at $t = 8$ h for the four symmetric bubble simulations: solid line is the thermal bubble at $r_b = 40$ km; dashed line is the thermal bubble at $r_b = 80$ km; dashed–dotted line is velocity bubble at $r_b = 40$ km; dotted line is the velocity bubble at $r_b = 80$ km.

and has downward motion along the center axis. This is significant because it induces warming throughout the vortex core (note Fig. 8d), rather than just in the vicinity of the positive θ tendencies. As the change in azimuthal wind speed reaches 2.42 m s^{-1} by this time, nonlinear dynamics would soon become important. These results show that during the exponential growth phase, the direct effects of the rapidly increasing eddy fluxes dominate secondary effects such as meridional circulations or symmetric gravity waves.

b. Adjusting, axisymmetrizing disturbances

The eddy flux tendencies were computed during the simulations of asymmetric temperature perturbations (Part I) and saved every 3 min of simulation time.[4] These time-dependent tendencies were then used as the forcing for symmetric perturbations to the tropical-storm-like vortex.

We examine in detail the effect of the $n = 3$ asymmetric warm bubble initialized at $r_b = 80$ km, $z_b = 5$ km on the tropical storm vortex (Part I, section 5b). The complexity of the dynamics is demonstrated by examining the eddy flux tendencies for u_0, v_0, and θ_0 at $t =$ 9 min, 30 min, 2 h, and 4 h, as shown in Figs. 9 and 10. At $t = 9$ min (Figs. 9a–c), the tendencies are dominated by the local interaction of the initial, asymmetric thermal perturbation with the basic-state vortex. However, as time evolves, the asymmetric thermal anomalies generate both asymmetric gravity waves and asymmetric vorticity anomalies, which then interact with the vorticity gradients of the basic-state flow. These wave–mean flow interactions generate new vorticity asymmetries, which quickly lead to more complicated tendencies, as shown for $t = 30$ min (Figs. 9d–f).

By $t = 2$ h (Figs. 10a–c) some features of the tendency fields can be more easily identified with the asymmetric processes described in Part I. Near the initial perturbation, there is an azimuthal tendency couplet associated with outward angular momentum transport caused by the favorable superposition of inner and outer potential vorticity (PV) anomalies (Part I, 3007–3010, and Fig. 17, $t = 2$ h; see the next section). In the core of the vortex, there is low- and midlevel acceleration associated with the axisymmetrization of low-level vorticity perturbations (Part I, Fig. 20). At higher altitudes near the axis, there is deceleration associated with transient growth caused again by favorable superposition of upper-level PV anomalies generated at early times but at different radii. By $t = 4$ h, the tendencies are dominated by momentum transports associated with the axisymmetrization of the remaining PV anomalies in all parts of the vortex (Figs. 10d–f). By this time, the tendency amplitudes are an order of magnitude lower than were observed in the first 30 min of evolution; however, these tendencies persist for approximately an order of magnitude longer.

The symmetric response to these tendencies is shown at $t = 30$ min, 2 h, and 6 h in Figs. 11–13. The fact that the symmetric response cannot be easily deduced by examining the tendencies alone is made abundantly clear in these figures. Consider the bull's-eye of negative v_0 at $t = 30$ min, $r = 50$ km, $z = 5$ km (Fig. 11c); it is not well collocated with the negative tendencies at $t = 9$ min, and there are positive tendencies in that area by $t = 30$ min. At $t = 2$ h, it seems impossible to connect

[4] In preliminary studies, these tendencies were saved only every 10 min. The symmetric dynamics that resulted had significant, qualitative differences from those for which the tendencies were saved every 3 min or less. It appears that the rapidly evolving nonhydrostatic dynamics of the asymmetric adjustment process has a significant impact on the symmetric response.

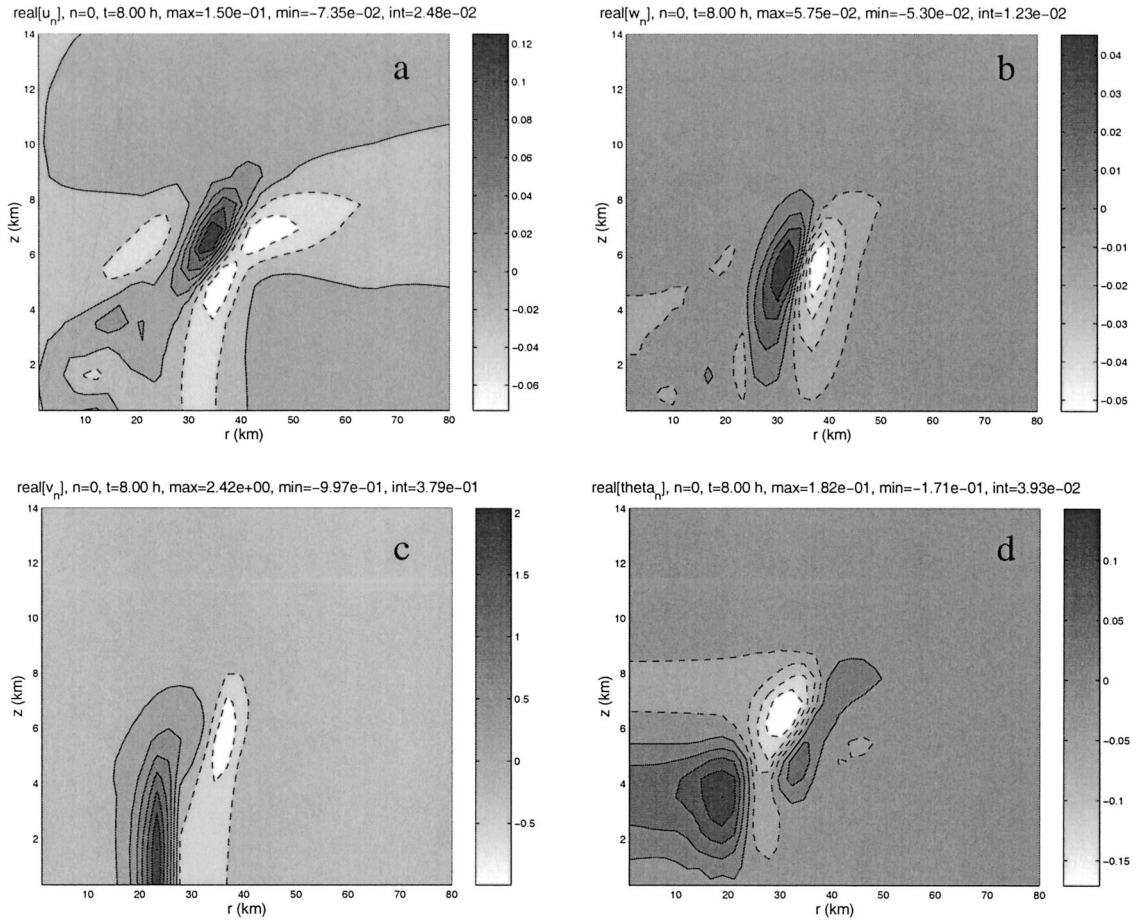

FIG. 8. Symmetric response at $t = 8$ h of the category 3 hurricane-like vortex to the eddy flux tendencies associated with the most unstable mode: (a) radial velocity; (b) vertical velocity; (c) azimuthal velocity; (d) potential temperature.

the regions of positive and negative perturbations with their corresponding tendencies. While the complexity of the asymmetric wave–mean flow interactions is responsible for the complexity of the tendency fields, the symmetric response is further complicated by the fact that symmetric changes induce secondary circulations and gravity waves, which themselves cause changes to the symmetric fields.

By $t = 6$ h, however, some discernable features reappear in the symmetric fields (Fig. 13). Clearly evident and persistent is a horseshoe-shaped region of positive v_0, with negative v_0 ''inside'' the horseshoe, indicating that there has been net inward, upward, and outward angular momentum transport from the location of the original perturbation. Also apparent in the u_0 and w_0 fields are a collection of outward-traveling gravity waves, strikingly similar to those seen in the symmetric forcing cases of section 3. By $t = 8$ h, the flow has equilibrated, and only decays slowly due to the effects of eddy viscosity. This equilibrated state is shown in terms of v_0 and θ_0 in Figs. 14a,b. Along with the vertically coherent, negative v_0 perturbations at $r = 60$ and $r = 25$ km, and positive v_0 perturbations at $r = 60$ and $r = 90$ km, there is a significant cooling in the upper levels of the vortex core. Also shown in Fig. 14 are the equilibrated changes resulting from simulations for $n = 3$ perturbations closer to the center, just outside the RMW at $r_b = 60$, and just inside the RMW at $r_b = 40$ km.

One would expect that upper-level cooling would have a negative impact on the central surface pressure, and this is confirmed in Fig. 15a, which shows the surface-center pressure perturbation as a function of time. It is clear that these impulsive, asymmetric temperature perturbations have ultimately led to net weakening of the tropical storm vortex. This is also made clear in Fig. 15b, which shows radial profiles of v_0 at the lowest level ($z = 320$ m) after $t = 8$ h. Also shown in Fig. 15 are results for perturbations at $r_b = 60$ km (dashed, both figures) and $r_b = 40$ km (dashed–dotted). All three cases lead to net increases in the central surface pressure, and net decreases in the maximum wind speeds. These results are summarized in Table 2.

As these predictions of vortex weakening by asymmetric forcing are seemingly at odds with many of the previous studies discussed in the introduction, addi-

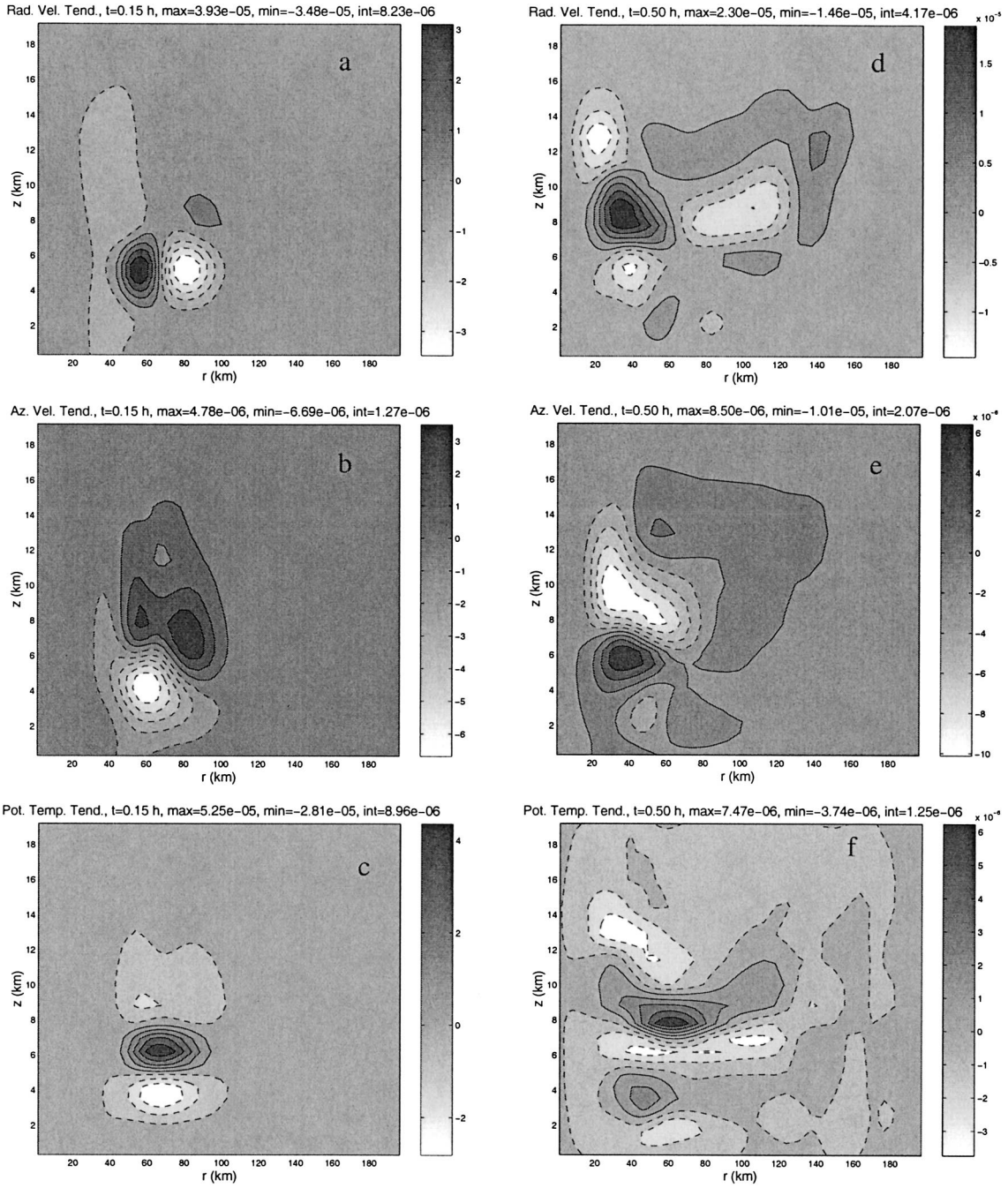

FIG. 9. Symmetric tendencies induced by the evolution of an $n = 3$ thermal asymmetry at $r_b = 80$ km, $z_b = 5$ km: (a) u_0 tendency, $t = 9$ min; (b) v_0 tendency, $t = 9$ min; (c) θ_0 tendency, $t = 9$ min; (d) u_0 tendency, $t = 30$ min; (e) v_0 tendency, $t = 30$ min; (f) θ_0 tendency, $t = 30$ min.

tional simulations were performed to evaluate the sensitivity of these results to the altitudes of the initial thermal asymmetries, their azimuthal wavenumber, and the strength of the diffusion.[5] Simulations with $z_b = 3$ km and $z_b = 7$ km are summarized in Fig. 16 and Table 2. For higher-altitude forcing, the results are similar, with universally positive pressure changes and negative surface velocity changes. Interestingly, the horseshoe shaped pattern of positive v_0, surrounding a core of negative v_0, is simply displaced upward about 2 km (not shown), such that the magnitudes of the pressure and

[5] The asymmetric dynamics were also resimulated with correspondingly lower viscosities.

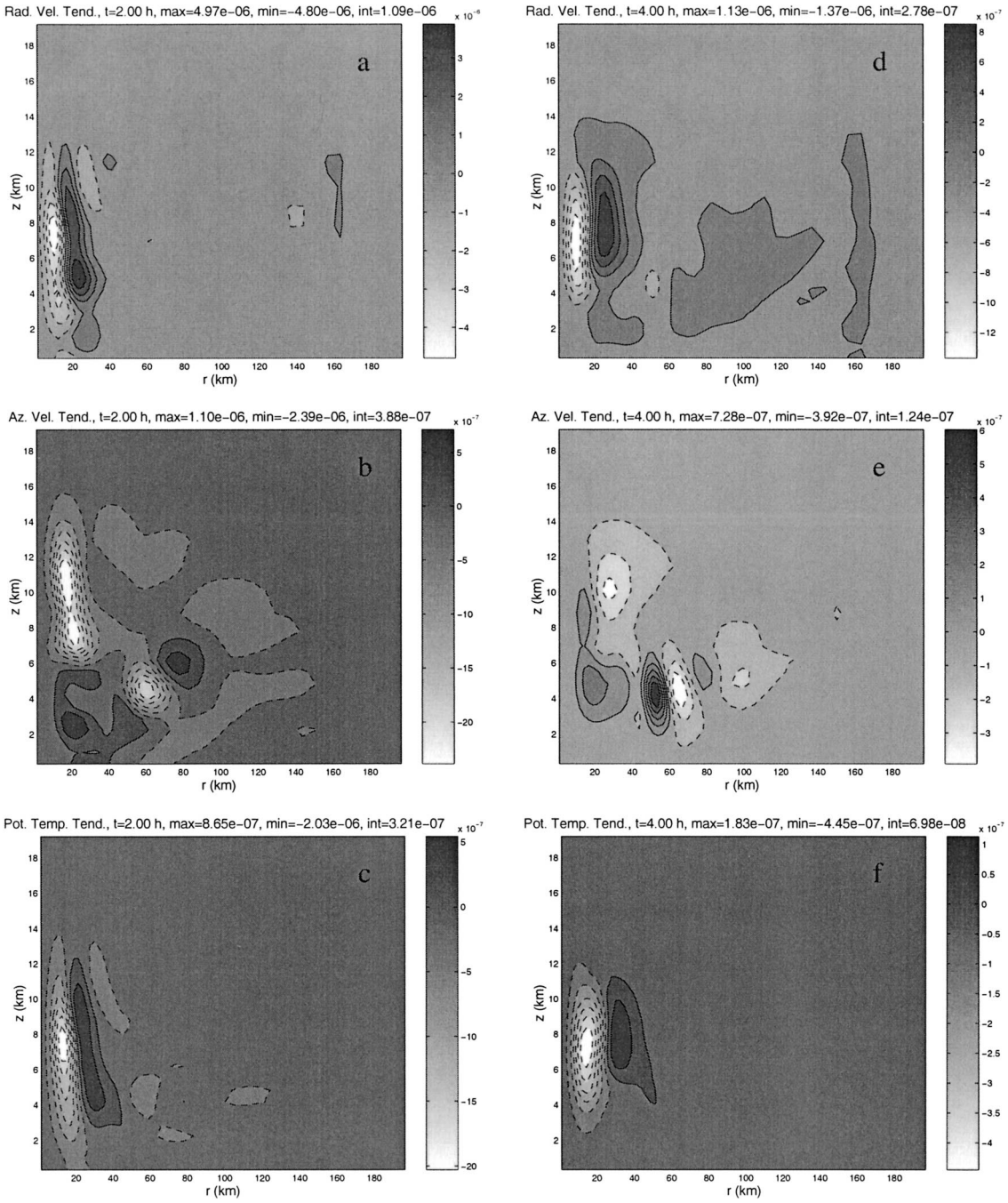

FIG. 10. Symmetric tendencies induced by the evolution of an $n = 3$ thermal asymmetry at $r_b = 80$ km, $z_b = 5$ km: (a) u_0 tendency, $t = 2$ h; (b) v_0 tendency, $t = 2$ h; (c) θ_0 tendency, $t = 2$ h; (d) u_0 tendency, $t = 4$ h; (e) v_0 tendency, $t = 4$ h; (f) θ_0 tendency, $t = 4$ h.

velocity changes at the surface are 2–4 times smaller than for $z_b = 5$ km. For lower altitude forcing, the horseshoe pattern is 2 km lower, and the velocity changes are 2–3 times larger. For $r_b = 40$ km and $z_b = 3$ km, the surface pressure actually decreases. In this case, however, the surface winds are still decreased at the RMW, though they are also substantially increased inside the RMW (Fig. 16b, dashed–dotted line). This negative–positive couplet of v_0 centered just inside the RMW represents a contraction of the vortex size, resulting in lower pressures. Conversely, for $r_b = 80$ and 60 km and $z_b = 3$ km, we find a small but positive change in v_0 at the RMW, and yet a small pressure increase. In these cases, the

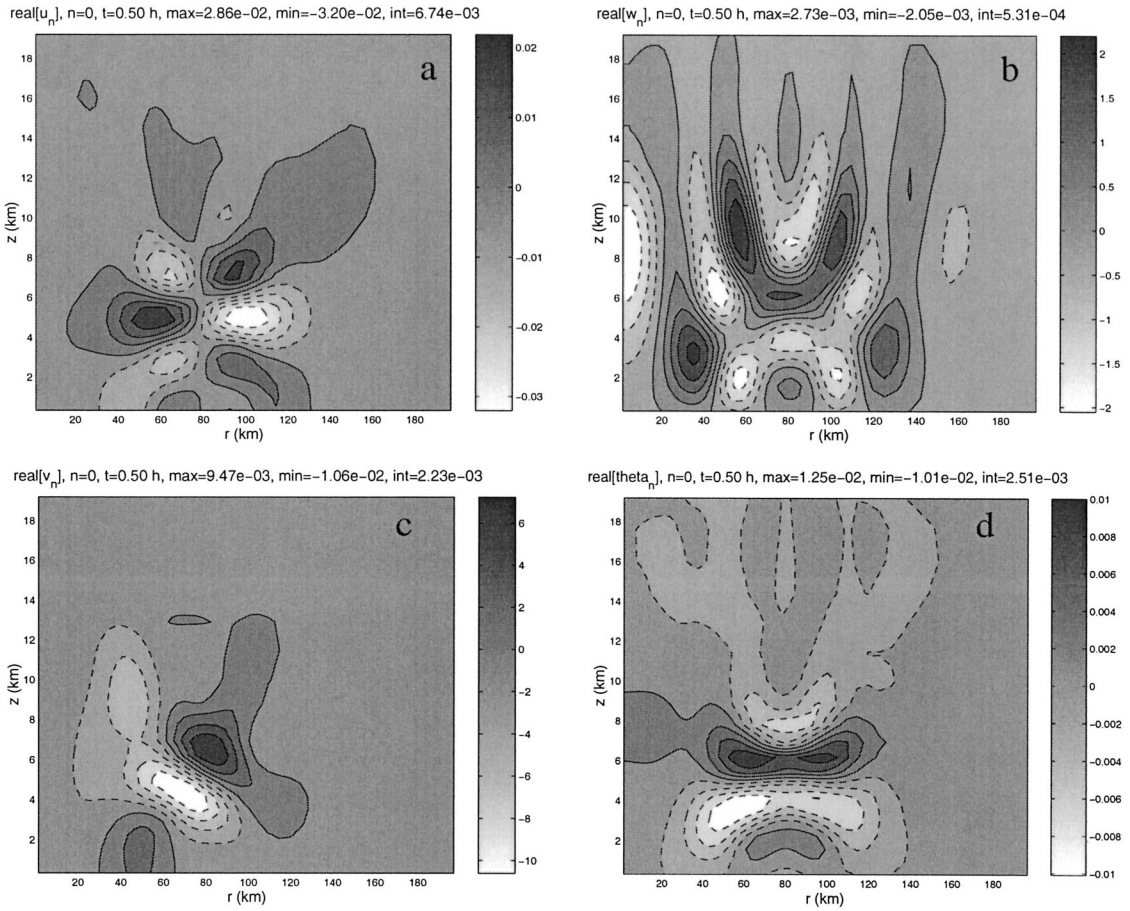

FIG. 11. Symmetric response to the tendencies caused by the asymmetric thermal bubble at $r_b = 80$ km, $z_b = 5$ km, at $t = 30$ min: (a) u_0, (b) w_0, (c) v_0, and (d) θ_0.

inner part of the positive v_0 horseshoe is coincident with the RMW.

Fig. 17 and Table 2 show that the responses are similar for wavenumbers $1 \leq n \leq 4$. For lower eddy viscosities ($\nu = 20$ and 10 m^2 s^{-1}), the pressure changes are nearly identical, with lower values and larger oscillations visible only in an expanded graph (Fig. 17c). The surface velocity changes have noticeably sharper features, due to decreased vertical and radial diffusion of momentum.

c. Understanding the results of asymmetric forcing

On a mechanical level, we can gain some understanding as to why asymmetric thermal perturbations do not lead to intensification. To first order, the perturbation PV field is

$$q_n = \frac{1}{\overline{\rho}}(\omega_n \cdot \nabla\overline{\theta} + \overline{\omega} \cdot \nabla\theta_n)$$

$$= \frac{1}{\overline{\rho}}\left(\xi_n\frac{\partial\overline{\theta}}{\partial r} + \eta_n\frac{1}{r}\frac{\partial\overline{\theta}}{\partial\lambda} + \zeta_n\frac{\partial\overline{\theta}}{\partial z} + \overline{\xi}\frac{\partial\theta_n}{\partial r} + \overline{\eta}\frac{1}{r}\frac{\partial\theta_n}{\partial\lambda} + \overline{\zeta}\frac{\partial\theta_n}{\partial z}\right), \quad (4.1)$$

where ξ, η, and ζ are the radial, azimuthal, and vertical components of the three-dimensional vorticity vector $\boldsymbol{\omega}$. For axisymmetric vortices without secondary circulations, $\overline{\eta}$ and $\partial\overline{\theta}/\partial\lambda$ are zero. When a thermal perturbation is introduced, ω_n is initially zero and only the fourth and sixth terms of the rhs of (4.1) contribute. In basic states without vertical shear, and in the quasigeostrophic limit, $\overline{\xi}$ is neglected and only the sixth term contributes; this is consistent with the notion that heating in the middle levels of the atmosphere generates high PV below and low PV aloft. However, the vortices studies here have substantial vertical wind shear, and for the asymmetric initial conditions studied in Part I, the radial-gradient PV is larger than the vertical-gradient PV. Figures 18a,b show the real parts (equivalent to a radial cross section in the positive x direction) of the PV contributions from radial and vertical gradients of θ_n in the original simulation for $n = 3$, $r_b = 80$ km from Part I (see also Fig. 15 of Part I). The radial-gradient PV is

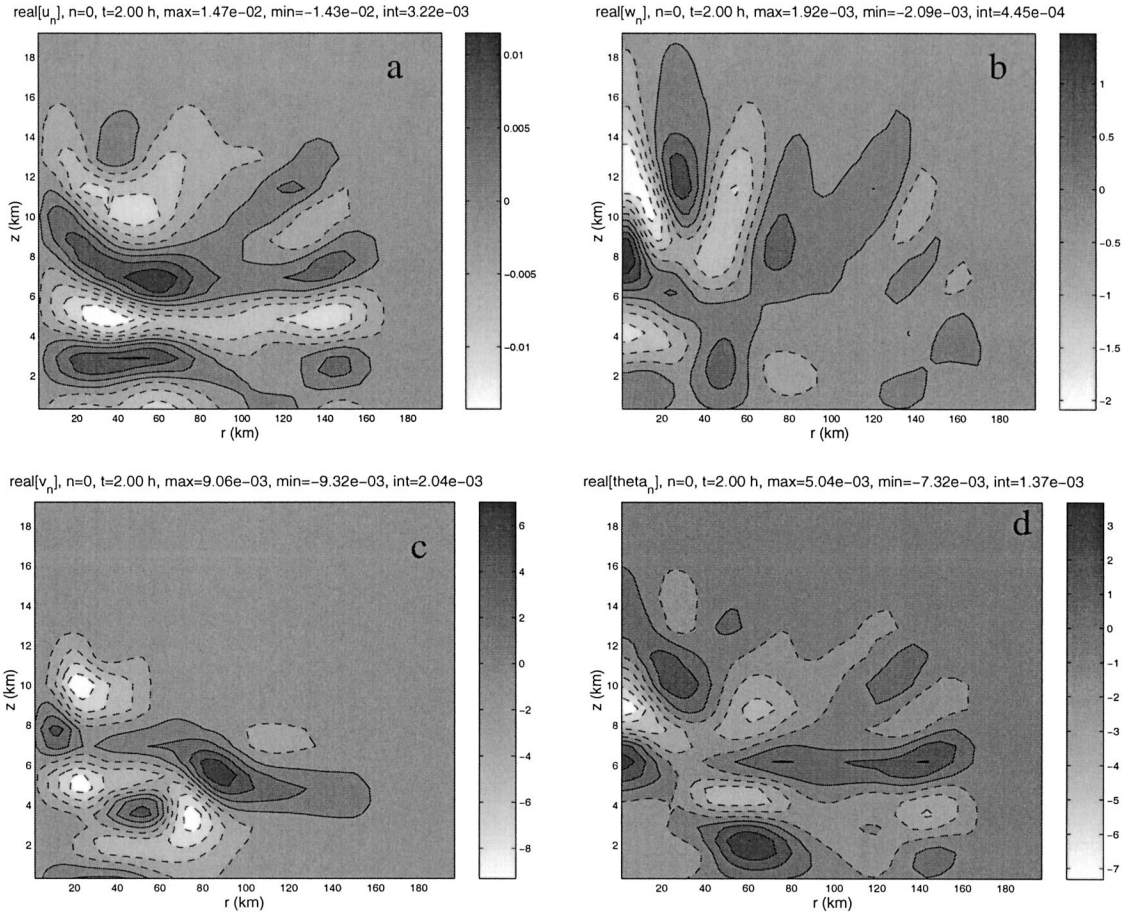

FIG. 12. As in Fig. 11, but at $t = 2$ h.

twice as large as the vertical-gradient PV, such that the axis of the PV dipole is more horizontal than vertical.

During the hydrostatic and gradient wind adjustment process, which is essentially completed in less than an hour, the total PV is redistributed from purely thermal PV to a mixture of vorticity and thermal PV. The quasi-balanced vorticity fields that develop have nearly the same shape as the PV fields, as shown in Fig. 18. In this configuration, the inner ring of vorticity perturbations are advected toward same-sign counterparts in the outer ring, leading to upshear tilt, downgradient momentum transport, and a transfer of kinetic energy from the basic state to the perturbations. For later times, the tilt is reversed and there is upgradient momentum transport, during which some of this energy may be returned to the basic state. This reversal of the momentum transport can be clearly seen in Figs. 10b and 10e. However, during this time some of this energy is redistributed through wave–mean flow interactions and also lost to dissipation.

Numerous previous studies have shown that when the initial PV or vorticity perturbations are balanced, and radially aligned, the evolution proceeds directly to axisymmetrization and there are only upgradient momentum transports (Carr and Williams 1989; Smith and Montgomery 1995; Montgomery and Kallenbach 1997; Nolan and Farrell 1999b; Montgomery and Enagonio 1998; Moller and Montgomery 1999, 2000; Shapiro 2000; Enagonio and Montgomery 2001). It is clear from our analysis that PV perturbations generated from asymmetric temperature perturbations have a different effect.

5. Nonlinear simulations

a. Numerical model, parameters, and initialization

To simulate the dynamics presented in Part I and above, we use the ''dynamic core'' of the Weather Research and Forecast model (WRF) version 1.2.1. WRF is a next-generation, regional, fully compressible model of the atmosphere presently under development by a number of agencies involved in atmospheric research and forecasting [the National Center for Atmospheric Research (NCAR) Mesoscale and Microscale Meteorology Division (MMM), the National Centers for Environmental Prediction (NCEP) Environmental Modeling Center (EMC), the National Oceanic and Atmospheric Administration (NOAA) Forecast Systems Lab-

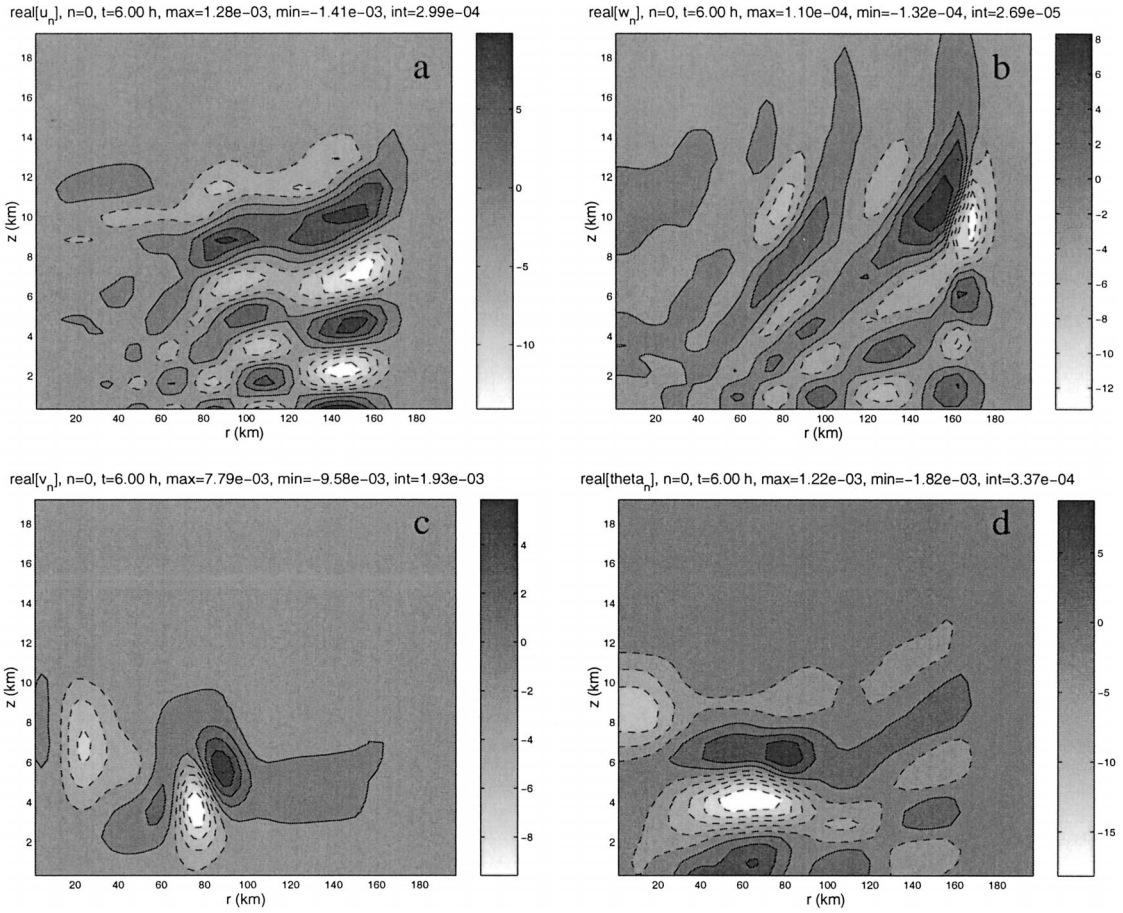

FIG. 13. As in Fig. 11, but at $t = 6$ h.

oratory (FSL) Forecast Research Division (FRD), the U.S. Air Force Weather Agency (AFWA), and University of Oklahoma (UOK) Center for the Analysis and Prediction of Storms (CAPS)], along with a number of university scientists (Michalakes et al. 2001). While its use as a reliable research and forecast tool for full-physics simulations is still a number of years in the future, the dynamic core (which solves the advection, diffusion, and compressibility terms) has undergone considerable evaluation (Wicker and Skamarock 2002; Takemi and Rotunno 2003).

The model domain is a square box, 600 km on each side, from $z = 0$ to 20 km. The horizontal grid spacing is constant, $\Delta x = \Delta y = 2$ km. There are 30 vertical levels, using the same stretching function as the 20 vertical levels used in the linear model (see Part I, appendix B). As in the linear simulations, the Coriolis parameter is a constant $f = 5.0 \times 10^{-5}\ \mathrm{s}^{-1}$. The upper and lower boundaries are free slip, and the data on the outer boundaries are fixed to the initial conditions. Gravity wave reflection from the outer boundaries is minimized by the use of Newtonian relaxation regions adjacent to the boundaries, where all fields within a certain distance of domain edges are relaxed back to the initial conditions with a spatially varying relaxation rate:

$$\mu = \begin{cases} 0 & d \geq D \\ \mu_{\max}\left(\dfrac{D-d}{D}\right)^2 & d < D, \end{cases} \tag{5.1}$$

where d is the distance to the nearest edge, D is the width of the damping regions, and the maximum damping rate is $\mu_{\max} = 1/\kappa_{\min}$. For the simulations here, we used $D = 40$ km with timescale $\kappa_{\min} = 120$ s. Upper-boundary relaxation damping regions like those used in the linear model are not presently available with WRF. The horizontal and vertical eddy viscosities are set to 40 $\mathrm{m}^2\ \mathrm{s}^{-1}$. An advective time step of 20 s was used, with six acoustic steps for each advective step. Vertical propagation of acoustic modes are solved implicitly.

To summarize, the nonlinear simulations are designed to match the linearized results with a larger domain, higher resolution, and fully compressible physics. Along with the absence of the upper damping region, there are two significant ways in which the design of the WRF

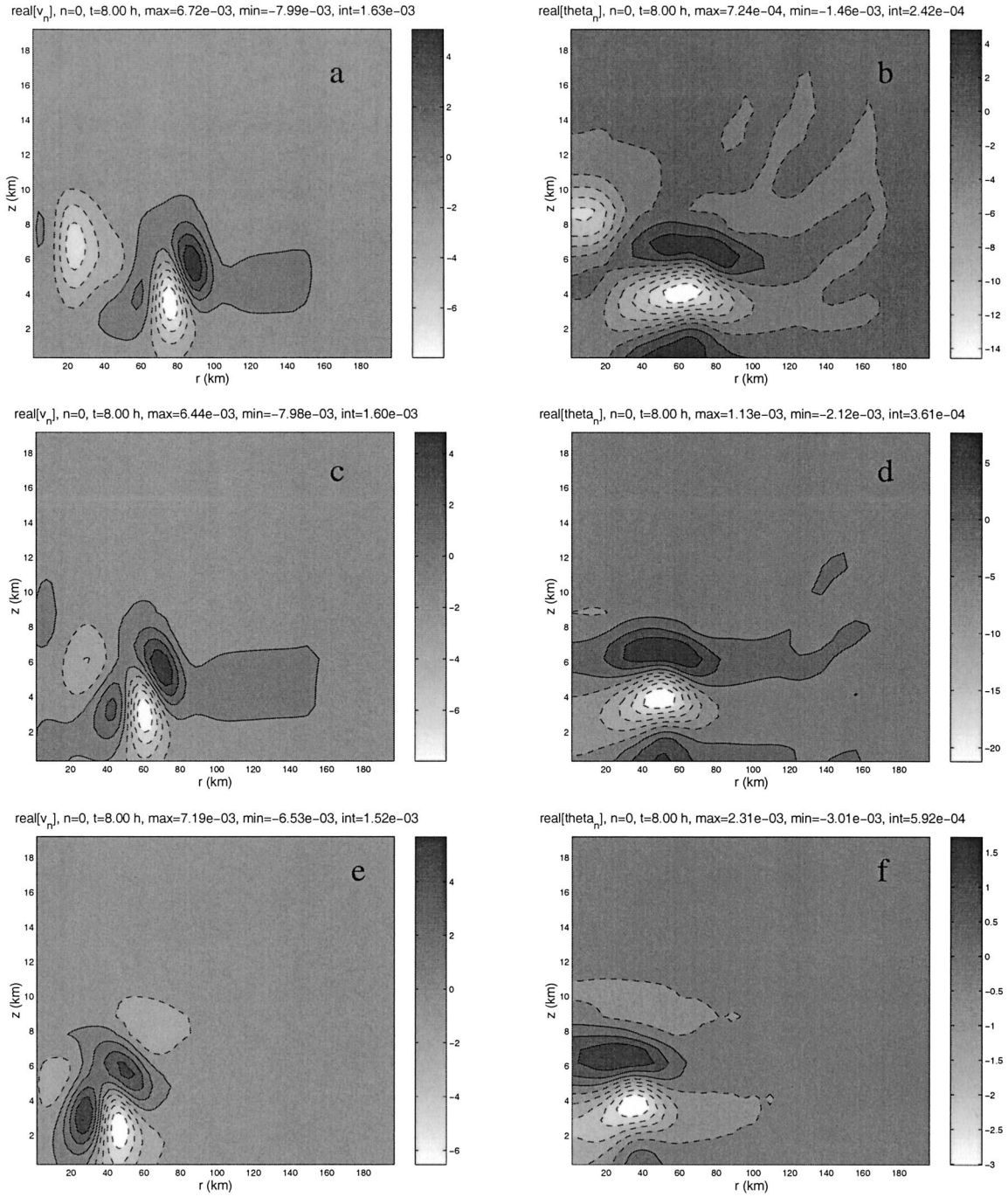

FIG. 14. Equilibrated ($t = 8$ h) symmetric response to asymmetric bubbles at different radii: (a) v_0 for $r_b = 80$ km; (b) θ_0 for $r_b = 80$ km; (c) v_0 for $r_b = 60$ km; (d) θ_0 for $r_b = 60$ km; (e) v_0 for $r_b = 40$ km; (f) θ_0 for $r_b = 40$ km.

simulations affects the results. In the linear model, the effect of diffusion is to cause all *perturbations* to decay, leaving the basic state fixed. However, the effect of diffusion in WRF is to cause the vortex to ''spin down,'' albeit slowly, but measurably over the course of 8 h. Secondly, the square domain and its square damping regions generate weak, but observable, stationary perturbations in a wavenumber-4 pattern, spiralling inward from the domain boundaries.

To account for these discrepancies, for *every* case below we ran two simulations: one with perturbations and one without, that is, axisymmetric initial conditions. The perturbations at each time are then defined to be the difference between the initially axisymmetric vortex

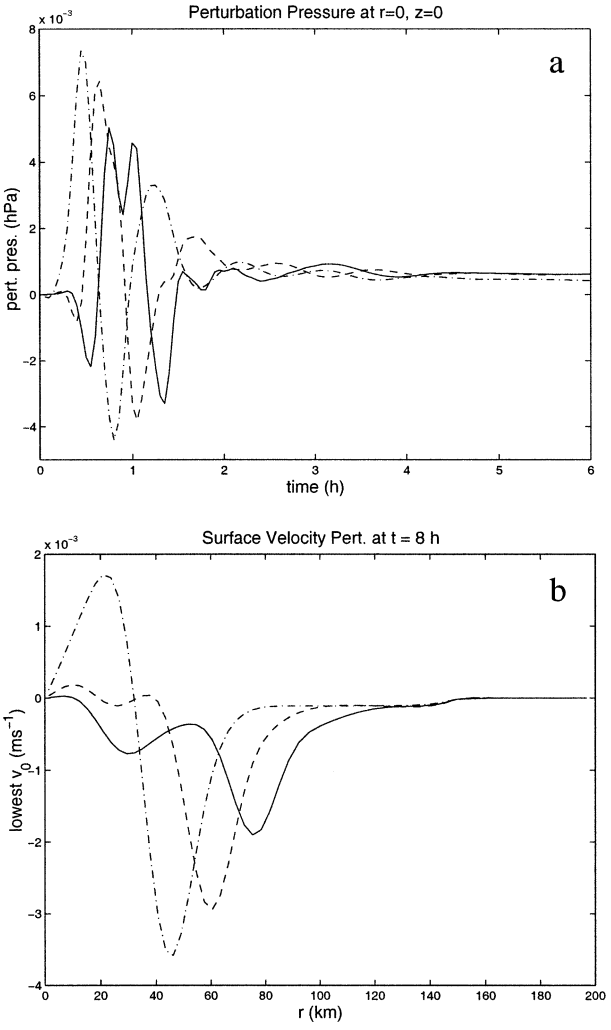

FIG. 15. Summary of results for asymmetric perturbations at different radii: (a) surface-center pressure perturbation with time for r_b = 80 km (solid), 60 km (dashed), 40 km (dashed–dotted); (b) as in (a), but for the change in surface winds at t = 8 h.

and a perturbed vortex. This produced results in remarkable agreement with the linear model.

b. An exponentially growing mode

The WRF model, with parameters described above, was initialized with the category 3 vortex (see Part I). In this and subsequent simulations, the axisymmetric basic states were linearly interpolated onto the three dimensional WRF grid. For this case, random perturbations were added to the zonal and meridional wind fields, in an annular region encompassing the RMW, with a normal distribution around 0 and a variance of 1 m s^{-1}.

The random noise in the inner-core wind field quickly excited the wavenumber-3 most unstable mode. The structure of the mode is clearly identified in the perturbation vertical velocity and vertical vorticity fields, as shown at t = 6 h in Fig. 19. The structure of the mode is very similar to that predicted in Part I (Fig. 5). Also shown in Fig. 19 are maximum perturbation vertical winds and vorticity as a function of time on a semilog plot, identifiying the growth as exponential up to about 8 h. The dashed–dotted line shows the growth rate predicted in Part I, in close agreement with the nonlinear results.

TABLE 2. Symmetric simulations of the tropical storm vortex with asymmetric forcing.

Forcing type	r_b (km)	z_b (km)	Surface-center Δp at t = 6 h (hPa)	Surface Δv at RMW at t = 6 h (m s^{-1})
n = 3 thermal perturbation, θ = 1 K	80	5	7.1×10^{-4}	-5.9×10^{-4}
	60	5	6.5×10^{-4}	-1.5×10^{-3}
	40	5	4.1×10^{-4}	-2.9×10^{-3}
	80	7	3.1×10^{-4}	-1.0×10^{-4}
	60	7	3.3×10^{-4}	-3.5×10^{-4}
	40	7	3.9×10^{-4}	-6.6×10^{-4}
	80	3	4.0×10^{-4}	1.8×10^{-3}
	60	3	2.2×10^{-4}	3.3×10^{-3}
	40	3	-1.2×10^{-3}	-1.2×10^{-2}
n = 1	40	5	3.8×10^{-4}	-2.3×10^{-3}
n = 2	40	5	1.5×10^{-4}	-3.3×10^{-3}
n = 4	40	5	4.2×10^{-4}	-2.2×10^{-3}
n = 3, ν = 20 m^2 s^{-1}	40	5	3.3×10^{-4}	-1.8×10^{-3}
n = 3, ν = 10 m^2 s^{-1}	40	5	2.7×10^{-4}	-8.7×10^{-4}

c. An adjusting, axisymmetrizing disturbance

The tropical storm vortex was used as the initial condition, and a wavenumber-3 temperature perturbation of the same structure as used in Part I [Eq. (5.1)], with r_b = 40 km, was added to the perturbed simulation.

The vortex evolved almost exactly as predicted by the linear model. First, outward-propagating spiral gravity waves were generated (Fig. 20a). This hydrostatic adjustment process leaves behind quasi-balanced vorticity perturbations that are advected and sheared by the basic-state flow (Fig. 20b; cf. Part I, Fig. 21a). These perturbations then interact with the symmetric vortex via eddy heat and momentum fluxes, inducing symmetric secondary circulations, ultimately leading to changes in the symmetric wind and temperature profiles (Figs. 20c and 20d; cf. Figs. 14e and 14f, above). For most of the domain, there is good agreement between the symmetric changes predicted by the linear model and the WRF simulation. The large velocity and temperature changes near the upper boundary are caused by reflections and interactions of upward-propagating gravity waves with the upper boundary, as the WRF simulation does not have an upper damping region. The agreement is very good for the surface-center pressure perturbations for simulations with r_b = 80, 60, and 40 km (Fig. 20e; cf. Fig. 15a).

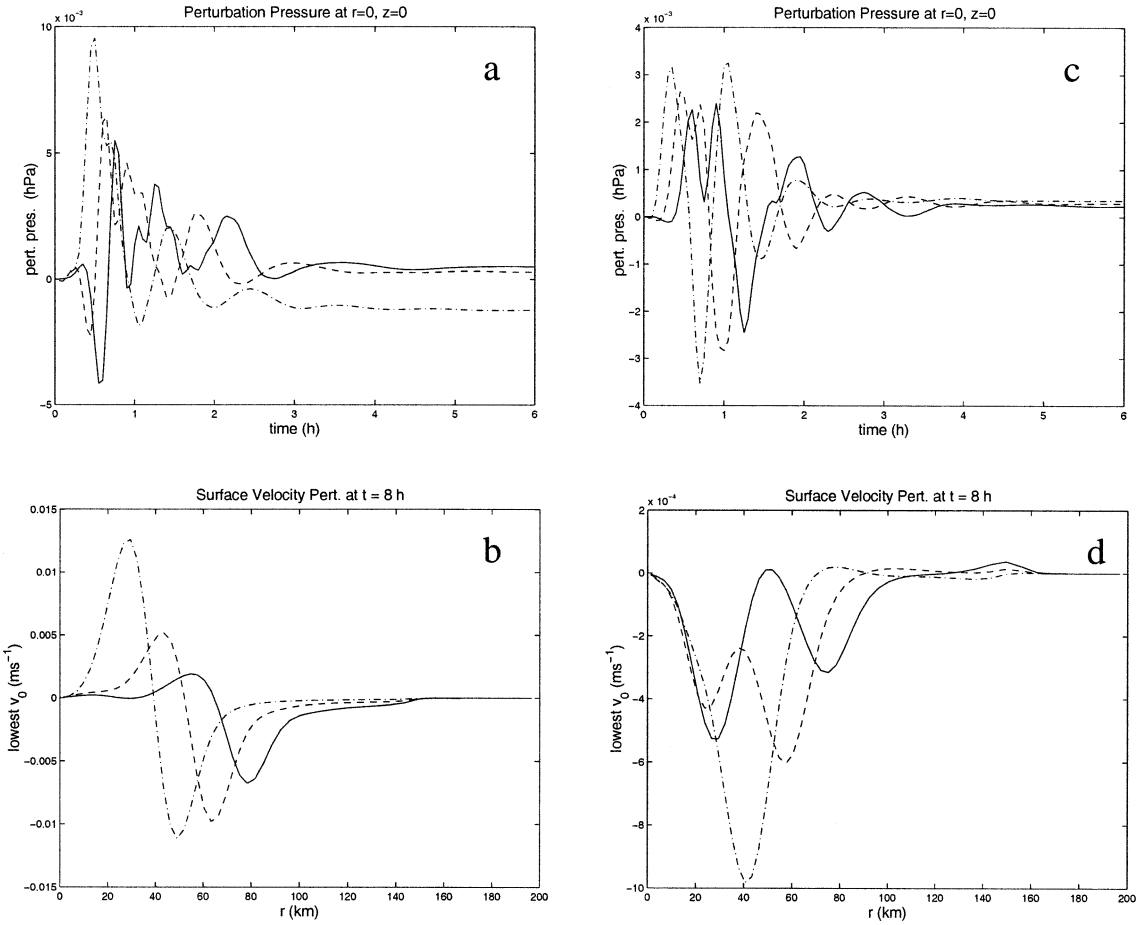

FIG. 16. As in Fig. 15, but for thermal asymmetries at different altitudes: (a) pressure change for $z_b = 3$ km; (b) surface velocity change for $z_b = 3$ km; (c) pressure change for $z_b = 7$ km; (d) surface wind change for $z_b = 7$ km. Plots are for $r_b = 80$ km (solid), 60 km (dashed), and 40 km (dashed–dotted).

d. A three-dimensional, localized thermal perturbation

In real tropical cyclones, the heat released from bursts of convection is almost entirely positive (although there could be regions of negative heating associated with evaporational cooling, etc.). The resulting temperature perturbation would then project strongly onto both symmetric and asymmetric dynamics. The cylindrical symmetry of the vortex allows the dynamics to be decomposed into symmetric and asymmetric parts; the asymmetric parts can be further decomposed by azimuthal wavenumber. Throughout this study, we have considered the dynamics separately in this manner. Does the final result of a fully nonlinear simulation equal the sums of the predictions from linear theory? And, more importantly, does convective heating away from the vortex center have a net positive or negative effect of the overall cyclone intensity?

To address these questions, the tropical-storm vortex in the WRF model was initialized with a thermal perturbation quite similar to those considered above, but localized in three-dimensional space:

$$\theta(x, y, z, t = 0) = \theta_0 \exp\left[-\frac{(x - x_b)^2 + (y - y_b)^2}{\sigma_r^2} - \frac{(z - z_b)^2}{\sigma_z^2}\right], \tag{5.2}$$

with $\theta_0 = 1$ K, $x_b = 40$ km, $y_b = 0$ km, and $z_b = 5$ km; $\sigma_r = 20$ km, and $\sigma_z = 2$ km, as before. The evolution of the resulting perturbations are shown in Fig. 21. We see the radiation of gravity waves and the development of quasi-balanced vorticity and temperature perturbations, which are axisymmetrized over time. The resulting ''final state,'' approximated by the fields at $t = 8$ h, is quite symmetric, and significantly, dominated by positive values in the perturbation vorticity and temperature fields. The surface-center pressure change is indeed ultimately negative, as shown in Fig. 22.

From our results, we can quickly estimate to what extent this intensity change is caused by the excitations of symmetric and asymmetric motions. In Fig. 7 and Table 1, the pressure change caused by a 1-K symmetric thermal bubble at $r_b = 40$ km is shown; the approximate

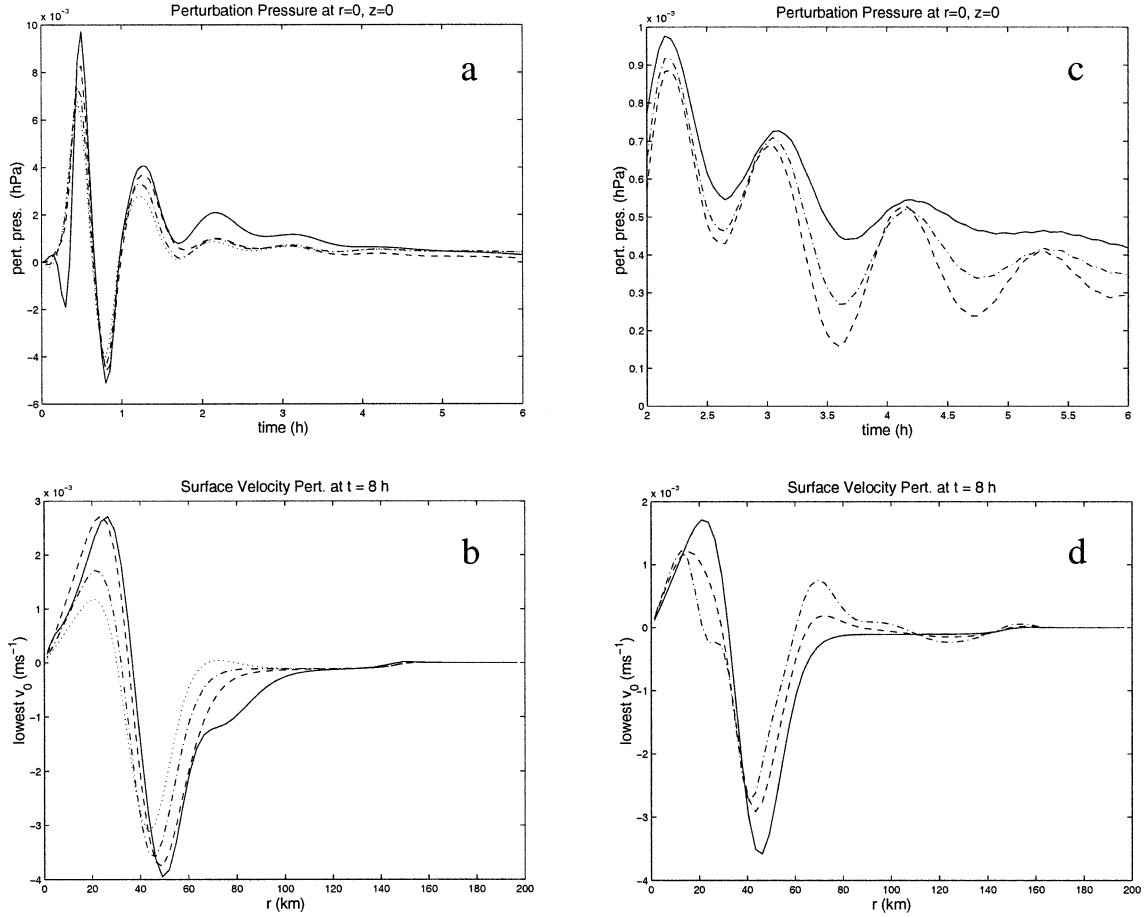

FIG. 17. As in Fig. 15, but for different wavenumbers and different viscosities, for $r_b = 40$ km, $z_b = 5$ km. (a), (b) Different azimuthal wavenumbers, with $n = 1$ (solid), $n = 2$ (dashed), $n = 3$ (dashed–dotted), and $n = 4$ (dotted); and (c), (d) different eddy viscosities, with $\nu = 40$ (solid), $\nu = 20$ (dashed), and $\nu = 10$ (dashed–dotted) m^2 s^{-1}. Note different axes for (c).

final change is -0.091 hPa. In Fig. 15 and Table 2, the pressure changes caused by 1-K asymmetric bubbles are shown; the final changes are all on the order of 4×10^{-4} hPa. The maximum amplitudes of the perturbations projected onto $n = 0$, 1, 2, 3, and 4 are 0.14, 0.27, 0.22, 0.16, and 0.10 K, respectively. We may conclude that *the intensity change caused by a localized, impulsive heat source is very closely approximated by the projection of that heat source onto the symmetric motions.*

This claim is also supported by additional linear and nonlinear simulations. Fig. 22a shows the surface-center pressure changes for localized, Gaussian heat sources at $x_b = 80$, 60, and 40 km in the WRF model. At $t = 6$ h, the pressure changes are -0.0021, -0.0057, and -0.017 hPa, respectively. Figure 22b shows the pressure changes from the projections of these thermal bubbles onto the symmetric fields in the linear model; the $t = 6$ h changes are -0.0020, -0.0051, and -0.014 hPa, respectively (see Table 2). The pressure falls are thus slightly larger in the nonlinear model, such that inclusion of the pressure changes from the asymmetries (which are positive) would not account for the small discrepancies. The pressure fall is nearly 10 times larger for the thermal bubble at $x_b = 40$ km than for the bubble at $x_b = 80$ km, which again shows the rapidly increasing impact of localized heating as it is brought toward the center of circulation (Shapiro and Willoughby 1982; Schubert and Hack 1982; Hack and Schubert 1986).

6. Conclusions

Using a three-dimensional, nonhydrostatic, but linear model, the dynamics of asymmetries to tropical-cyclone-like vortices caused by instantaneous symmetric and asymmetric temperature perturbations have been analyzed. In Part I, these disturbances were shown to evolve through a two-part adjustment process. First, there is hydrostatic and gradient wind adjustment, with the development of quasi-balanced vorticity perturbations, and the outward radiation of fast-moving gravity waves, which show little interaction with the basic state in the far field. Second, these quasi-balanced vorticity perturbations are sheared by the basic-state flow, causing time-evolving eddy heat and momentum fluxes as

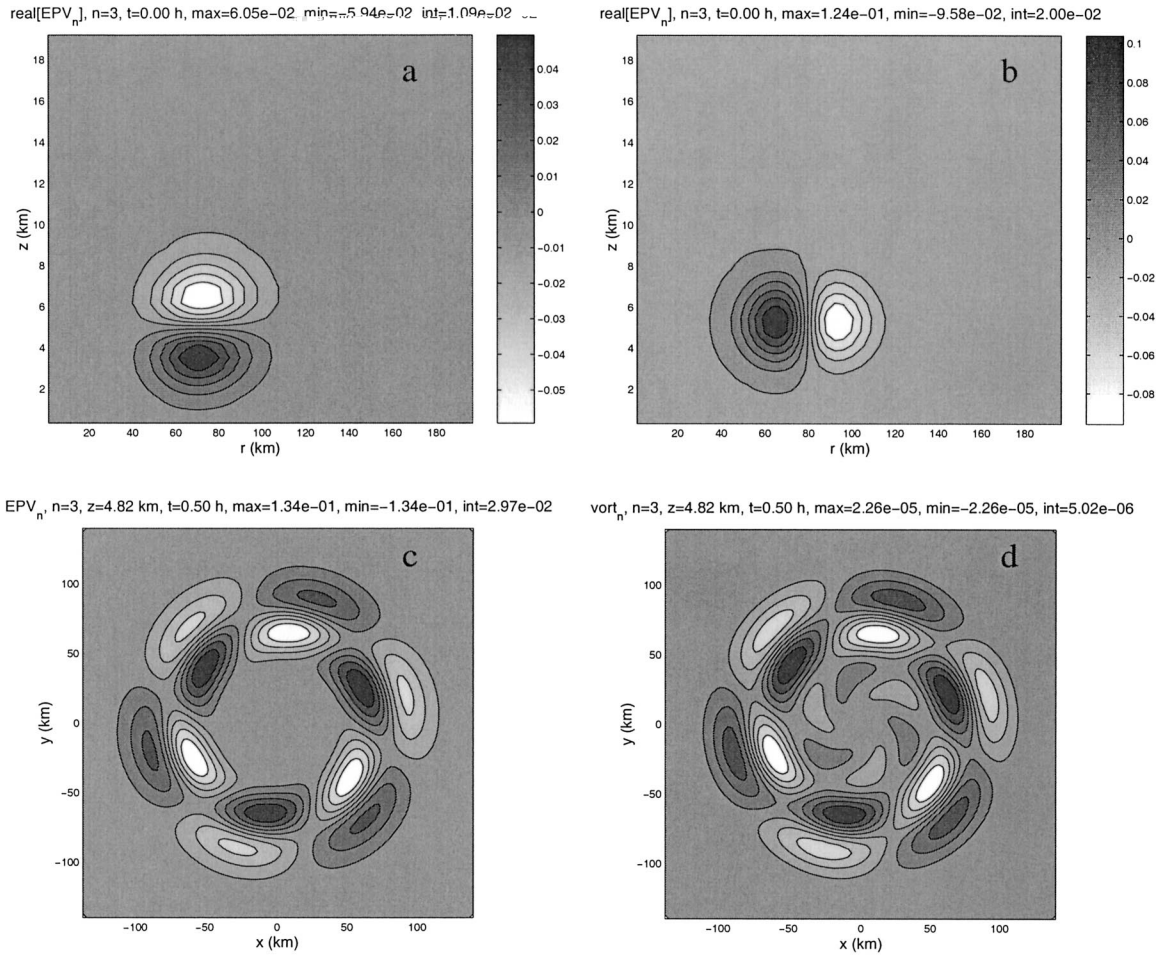

FIG. 18. Vorticity and PV in an asymmetric simulation from Part I: (a) PV from the radial gradient of θ; (b) PV from the vertical gradient of θ; (c) horizontal cross section at $z = 4.82$ km of PV at $t = 0.5$ h; (d) cross section of vorticity at the same time.

they are axisymmetrized. In this paper, we have demonstrated a third part of the adjustment process, which is the adjustment of the symmetric vortex to the heat and momentum eddy fluxes, resulting in additional (symmetric) gravity wave radiation, symmetric circulations, and ultimately a change in the wind and temperature fields of the symmetric vortex. A conceptual map of these processes is shown in Fig. 23. The arrows represent the flow of energy from localized convection, to asymmetric and symmetric heating, to asymmetric and symmetric motions, ultimately leading to intensity and structure changes of the symmetric vortex.

In a number of earlier works, it has been shown that the introduction of balanced vorticity asymmetries into or near the vortex core ultimately leads to an intensification of the vortex, particularly in regards to its maximum wind speed. In Part I and here, we have proceeded from the other end of the spectrum of balanced to unbalanced motions by using instantaneous temperature perturbations; in essence we have studied the hydrostatic and gradient-wind adjustment problem for temperature perturbations to three-dimensional balanced vortices. While the asymmetric/symmetric adjustment process always leads to increased wind speeds near the locations of the initial perturbations (aloft), we find that the net effect on the greater vortex is to decrease its intensity, in terms of either the maximum surface wind or the minimum surface pressure. The only exceptions were found when the thermal perturbations were initialized at a lower altitude (3 km), in which case there were either pressure falls or wind increases at the RMW, but not both.

A careful examination of the PV and vorticity fields generated by asymmetric temperature perturbations showed that they went through a period of transient growth before axisymmetrizing, which is perhaps responsible for the net weakening of the symmetric vortex. The differences between the effects of asymmetric vorticity and temperature perturbations can hopefully be explained on a deeper level, perhaps because temperature perturbations introduce potential energy to the vortex (some of which is converted to kinetic energy in the adjustment process), while vorticity perturbations introduce kinetic energy directly. This certainly deserves further study.

Symmetric initial perturbations were also considered.

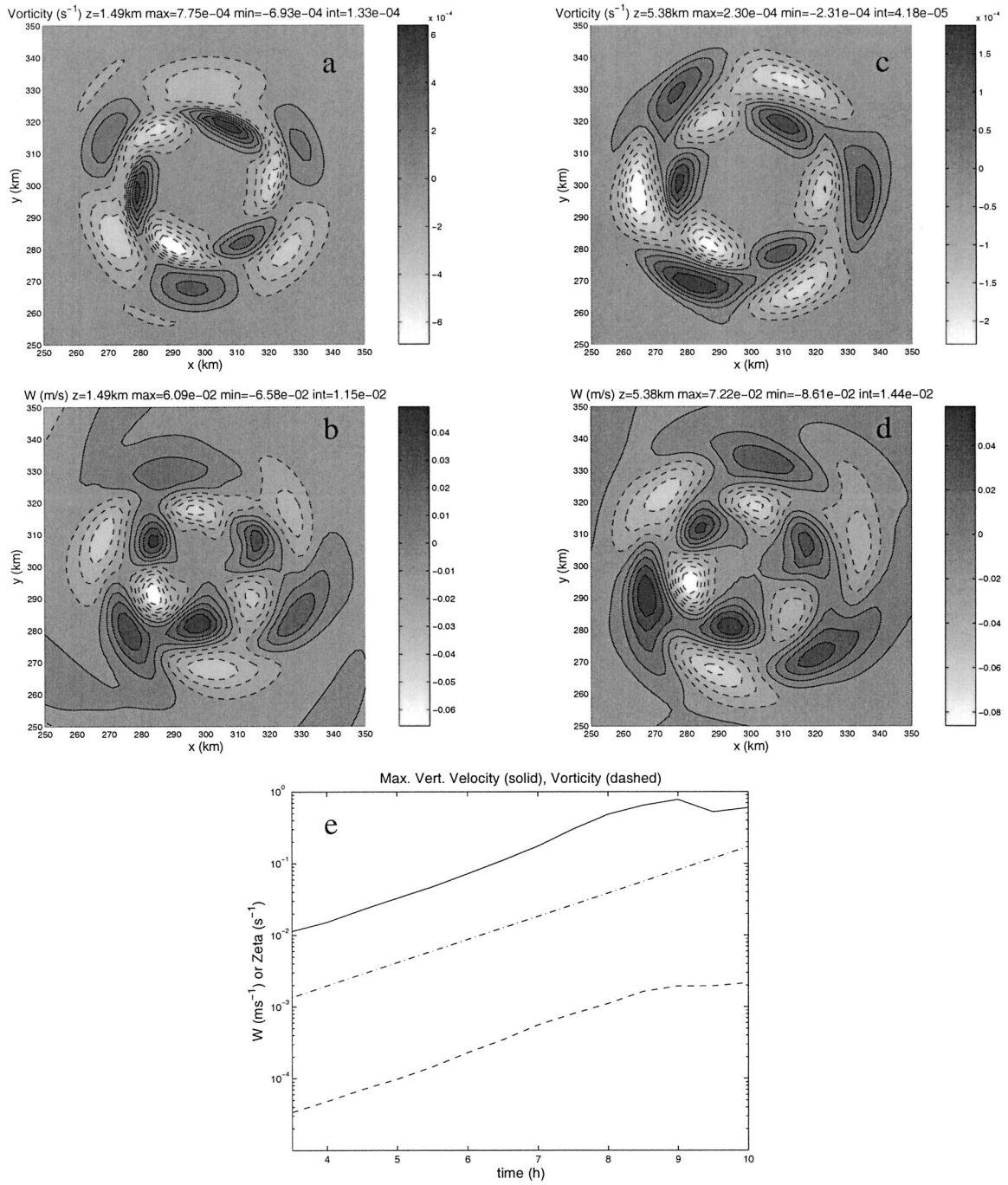

FIG. 19. WRF simulation of the most unstable mode in the category 3 vortex. Shown are (a) perturbation vertical vorticity and (b) velocity at $z = 1.49$, and (c), (d) at 5.38 km. (e) The maximum perturbation vorticity (dashed) and velocities (solid) at $z = 5.38$ km, as compared to the growth rate of the unstable mode computed in the linear model (dashed–dotted).

They were shown to go through a similar adjustment process, and were found to cause an increase in the symmetric wind field in the vicinity of the initial perturbation, including down to the surface, along with midlevel warming in the core and a decrease in the central surface pressure (for positive perturbations). Momentum perturbations were shown to have an effect very similar to temperature perturbations. Symmetric temperature perturbations were shown to cause a surface pressure change two orders of magnitude larger than asymmetric perturbations of equal amplitude. We thus conclude that the net effect of impulsive heating displaced from the vortex center is closely approximated by the projection of that heating onto the symmetric motions. High-resolution simulations with a

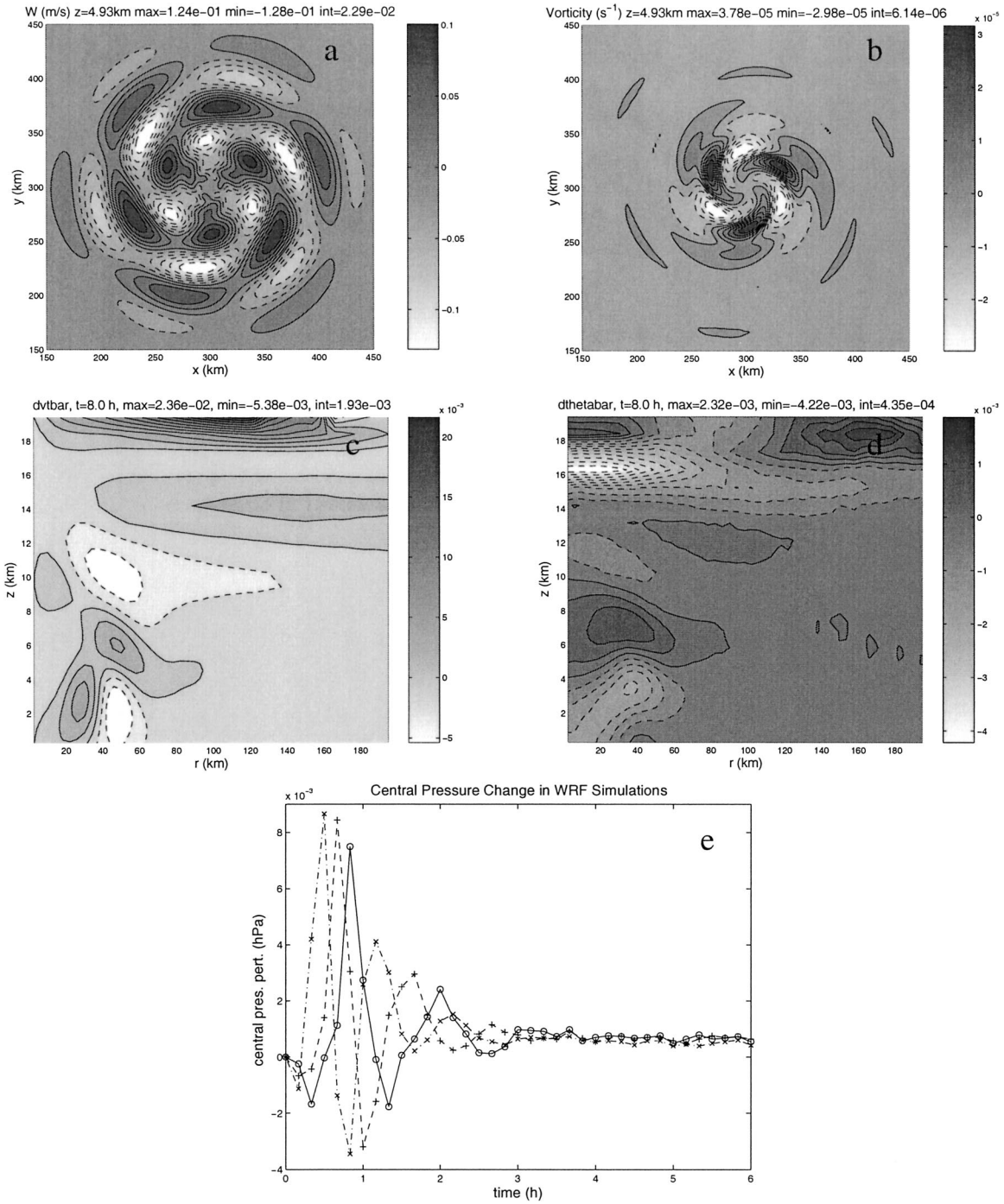

FIG. 20. WRF simulation of an $n = 3$ temperature perturbation at $r_b = 40$ in the tropical storm vortex: (a) vertical velocities at $z = 4.93$ km, $t = 30$ min; (b) vertical vorticity at $z = 4.93$ km, $t = 2$ h; (c) change in symmetric azimuthal velocity at $t = 8$ h; (d) change in symmetric potential temperature at $t = 8$ h; (e) central surface pressure change with time for $r_b = 80$ km (solid), 60 km (dashed), 40 km (dashed–dotted).

fully compressible, nonlinear model (the dynamic core of WRF) confirmed these conclusions for both purely asymmetric and localized (mixed symmetric and asymmetric) thermal perturbations.

Further study is necessary before these results can be unconditionally applied to real tropical cyclones. The effects of a number of features specific to our simulations should be considered.

1) All simulations in both models used very simplistic,

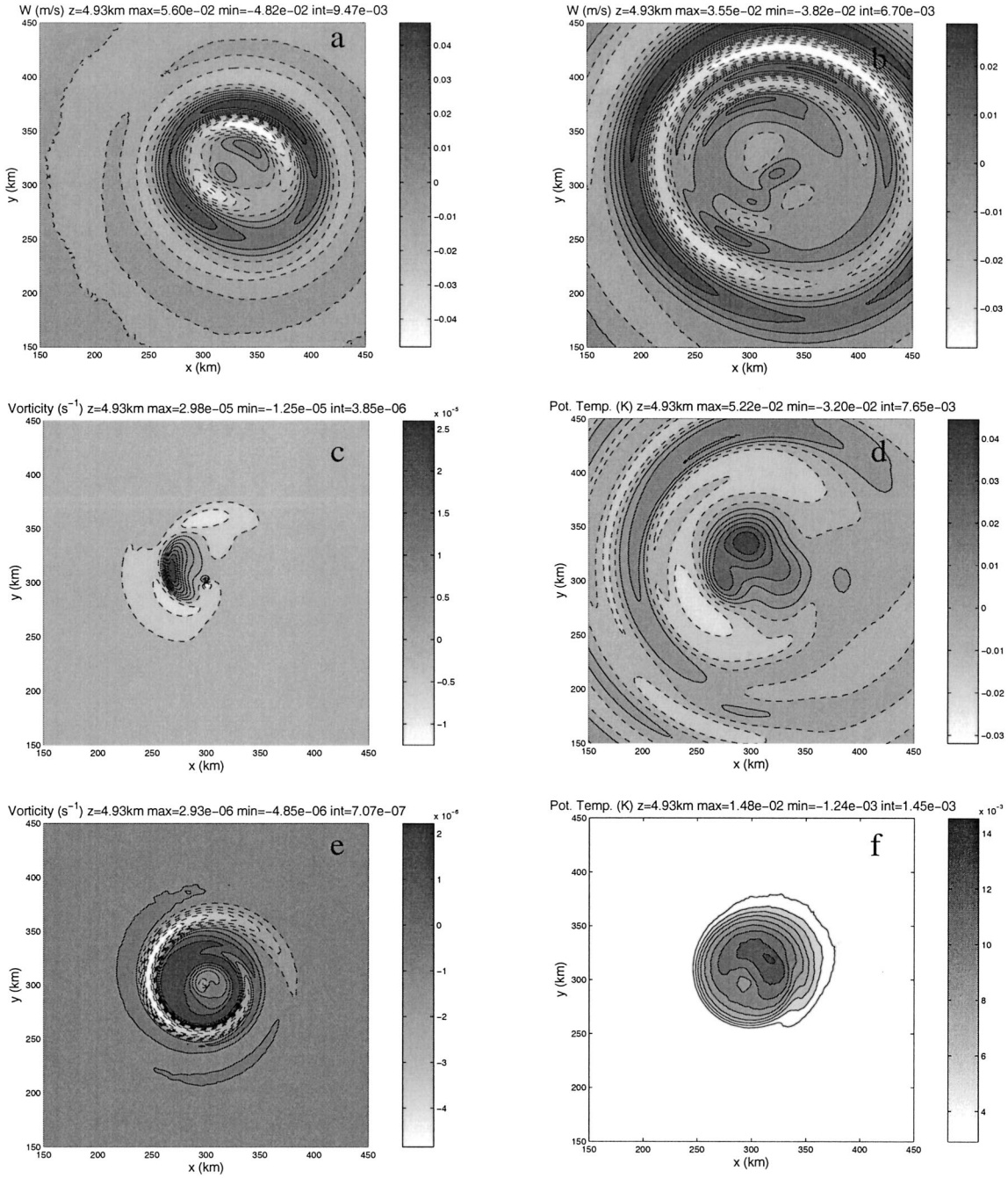

FIG. 21. Evolution of a Gaussian-shaped thermal perturbation at $x_b = 40$ km simulated in the WRF model: (a) w at $t = 30$ min and (b) $t = 1$ h; (c), (d) ζ and θ perturbations at $t = 2$ h; (e), (f) ζ and θ perturbations at $t = 8$ h. All data is at $z = 4.93$ km.

and probably overly large, diffusion. The large value of $\nu = 40$ m^2 s^{-1} was used to be consistent with the results in Part I; in that paper, $\nu = 40$ m^2 s^{-1} was used for the simulations of $n = 3$ asymmetries in the tropical storm vortex so that they could be compared to $n = 3$ perturbations to the category 1 hurricane-like vortex, which was unstable for lower viscosities. However, simulations with $\nu = 20$ and 10 m^2 s^{-1} did give very similar results (cf. Fig. 17).

2) Only a single type of spatial structure was used for the thermal perturbations. It is possible that thermal perturbations that are more closely matched to the temporally and spatially evolving latent heat release in actual convective outbreaks would give different results, particularly for the asymmetric dynamics.
3) The ''rapid'' heat release associated with localized convection events were approximated with instantaneously introduced perturbations to the asymmetric

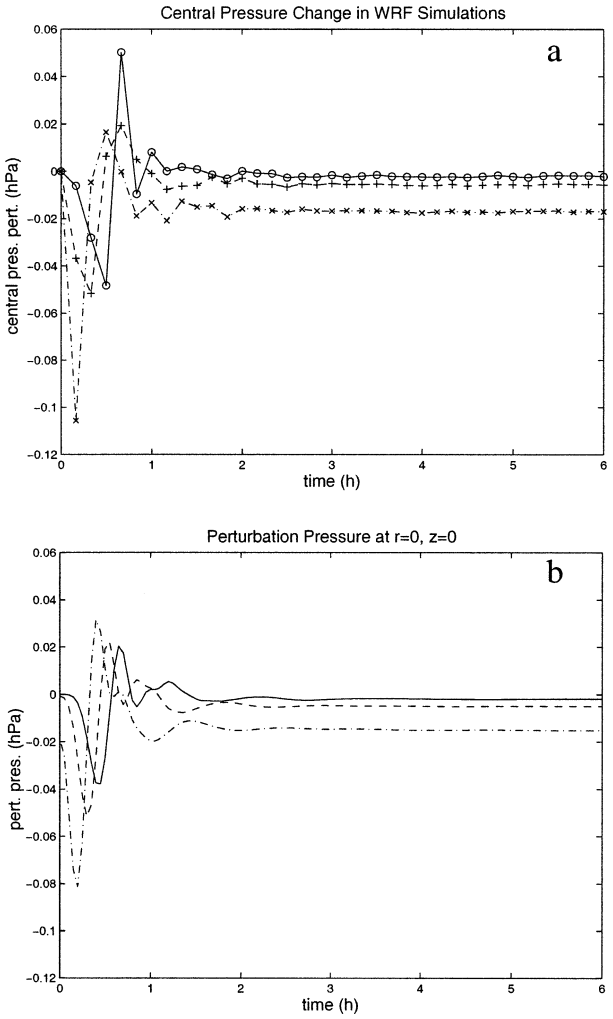

FIG. 22. Surface-center pressure perturbation in (a) WRF simulations, and (b) symmetric, linear model simulations of the symmetric projections of the localized thermal bubbles. Plots are for bubbles located at x_b = 80 km (solid), 60 km (dashed), and 40 km (dashed–dotted).

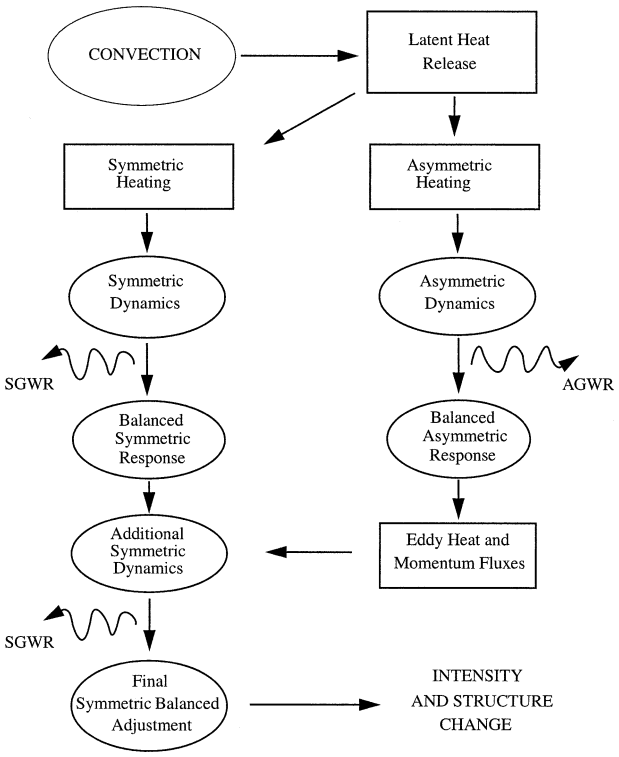

FIG. 23. Conceptual diagram of the dynamics studied in Part I and this study. Convection leads to symmetric intensity change through both symmetric and asymmetric processes. SGWR and AGWR are symmetric and asymmetric gravity wave radiation, respectively. Ellipses are motions, and rectangles are forcings.

temperature fields.[6] As discussed in Part I and section 4c, the PV anomalies generated by the asymmetric initial conditions have an ''upshear-tilted'' orientation, which leads to a period of transient growth, thus acquiring energy from the mean flow. It is possible that a more accurate depiction of the temporal evolution of latent heat release could change the results, particularly in regard to the asymmetries and their effects. Convective outbreaks are often associated with strong boundary layer coupling and significant vertical wind speeds, which may generate more vertically coherent PV anomalies on a short timescale, similar to those used in previous studies (e.g., Montgomery and Enagonio 1998, section 3b, cf. Part I, Fig. 15; see also Möller and Montgomery 2000; Shapiro 2000), which do not experience a period of transient growth and proceed directly to axisymmetrization. The detailed thermal and vorticity structures generated by convection in tropical cyclones is a topic of ongoing observational and numerical investigation (e.g., Feuer et al. 2002; Eastin 2002; Yang et al. 2002; Braun 2002; Zhang et al. 2002).

4) These basic-state vortices lack the frictionally and convectively induced secondary circulations that are well-known to be critical in determining the low-level structure and intensity of tropical cyclones. The secondary circulation may also change the stability and evolution of perturbations, and thus ultimately the wave–mean flow interactions, as has been indicated in previous studies (Nolan and Farrell 1999a,b; Nolan 2001).

Each of these issues will be addressed in future work.

[6] For symmetric and asymmetric perturbations separately, the equilibrated final state does not depend on the temporal distribution of the forcing: a short burst of heating has the same final effect as a longer period of heating with the same structure. This is *not* true for the symmetric response to asymmetric forcing, as the eddy fluxes are second-order quantities and their associated symmetric forcing is nonlinear. However, if the timescale of asymmetric forcing is short enough compared to the adjustment timescale, roughly less than 30 min, the results are indistinguishable from impulsive forcing. Furthermore, because the total response is dominated by the symmetric dynamics, the temporal evolution of the heating is not important.

Preliminary results using the asymmetric tornado equations (see Part I) have shown how radial variation of vertical winds can change the growth rates and structures of unstable modes in a vortex with a vertical jet (Nolan and Montgomery 2002a). This work will be extended to apply to both asymmetric and symmetric dynamics in tropical cyclones with realistic secondary circulations. Simulations with fully nonlinear models of increasing complexity are also under development. It is worth noting that two recent studies of Hurricane Opal, using the Geophysical Fluid Dynamics Laboratory Hurricane Prediction System, found that asymmetric intensification mechanisms had small impact compared to symmetric mechanisms during Opal's rapid intensification (Möller and Shapiro 2002; Persing et al. 2002).

In the hydrostatic and gradient adjustment process, some fraction of the potential energy associated with the original thermal perturbations is converted into kinetic and potential energy of the balanced asymmetries that are generated; some is also lost due to gravity wave radiation. The energy of these asymmetries is then in turn transferred to the symmetric vortex, with some loss due to to the symmetric adjustment process and friction. These energy exchanges (neglecting friction) are outlined in Fig. 23. A systematic and quantitative evaluation of these energy exchanges would be a useful contribution to our understanding of the intensification process. This will require energy equations for the nonhydrostatic, symmetric, and asymmetric motions, similar to those presented by Wang (2002), and remains for future work.

Acknowledgments. The authors would like to thank Prof. M. Montgomery and Dr. T. DelSole for many helpful discussions, and three anonymous reviewers for their valuable comments on the text. Much of this work was completed while the first author was a Visiting Scientist at the Princeton Program for Atmospheric and Oceanic Sciences and the Geophysical Fluid Dynamics Laboratory (GFDL), supported by NOAA and Princeton University. All the WRF simulations were performed on the GFDL High Performance Computing System as part of an ongoing collaboration with GFDL and NOAA. We also thank the WRF developers for their assistance. This work was also supported by the NSF under Grant ATM-0132006, and by the University of Miami.

APPENDIX A

The Reduced Symmetric Tornado–Hurricane Equations

We reduce the original five STHE to three coupled, linear equations. The pressure terms may be eliminated by multiplying both (2.1) and (2.3) by $\overline{\rho}$, then subtracting $\partial/\partial r$ of (2.3) from $\partial/\partial z$ of (2.1). After some rearrangement, we have

$$\begin{aligned}
&\frac{\partial \eta_0}{\partial t} + \overline{u}\left(\frac{\partial \overline{\rho}}{\partial z}\frac{\partial u_0}{\partial r} + \overline{\rho}\frac{\partial^2 u_0}{\partial r \partial z} - \frac{\partial \overline{\rho}}{\partial r}\frac{\partial w_0}{\partial r} - \overline{\rho}\frac{\partial^2 w_0}{\partial r^2}\right)\\
&\quad + \overline{w}\left(\frac{\partial \overline{\rho}}{\partial z}\frac{\partial u_0}{\partial z} + \overline{\rho}\frac{\partial^2 u_0}{\partial z^2} - \frac{\partial \overline{\rho}}{\partial r}\frac{\partial w_0}{\partial z} - \overline{\rho}\frac{\partial^2 w_0}{\partial r \partial z}\right)\\
&\quad + u_0\left(\frac{\partial \overline{\rho}}{\partial z}\frac{\partial \overline{u}}{\partial r} + \overline{\rho}\frac{\partial^2 \overline{u}}{\partial r \partial z} - \frac{\partial \overline{\rho}}{\partial r}\frac{\partial \overline{w}}{\partial r} - \overline{\rho}\frac{\partial^2 \overline{w}}{\partial r^2}\right)\\
&\quad + w_0\left(\frac{\partial \overline{\rho}}{\partial z}\frac{\partial \overline{u}}{\partial z} + \overline{\rho}\frac{\partial^2 \overline{u}}{\partial z^2} - \frac{\partial \overline{\rho}}{\partial r}\frac{\partial \overline{w}}{\partial z} - \overline{\rho}\frac{\partial^2 \overline{w}}{\partial r \partial z}\right)\\
&\quad + \overline{\rho}\left(\frac{\partial \overline{u}}{\partial z}\frac{\partial u_0}{\partial r} + \frac{\partial \overline{w}}{\partial z}\frac{\partial u_0}{\partial z} + \frac{\partial \overline{u}}{\partial r}\frac{\partial u_0}{\partial z} + \frac{\partial \overline{u}}{\partial z}\frac{\partial w_0}{\partial z}\right.\\
&\qquad \left. - \frac{\partial \overline{u}}{\partial r}\frac{\partial w_0}{\partial r} - \frac{\partial \overline{w}}{\partial r}\frac{\partial w_0}{\partial z} - \frac{\partial \overline{w}}{\partial r}\frac{\partial u_0}{\partial r} - \frac{\partial \overline{w}}{\partial z}\frac{\partial w_0}{\partial r}\right)\\
&\quad = \frac{\partial}{\partial z}\overline{\rho}[(2\overline{\Omega} + f)v_0 + F_u + E_u]\\
&\qquad - \frac{\partial}{\partial r}\overline{\rho}\left(\frac{g}{\overline{\theta}}\theta_0 + F_w + E_w\right),
\end{aligned} \tag{A.1}$$

where η_0 is a density-weighted azimuthal vorticity, related to the velocities and streamfunction by

$$\begin{aligned}
\eta_0 &= \frac{\partial}{\partial z}\overline{\rho}u_0 - \frac{\partial}{\partial r}\overline{\rho}w_0\\
&= -\frac{1}{r}\frac{\partial^2 \psi_0}{\partial r^2} - \frac{1}{r}\frac{\partial^2 \psi_0}{\partial z^2} + \frac{1}{r^2}\frac{\partial \psi_0}{\partial r},
\end{aligned} \tag{A.2}$$

when using (2.6).[A1] The lhs of (A.1) may also be rearranged into a form that describes the advection and basic-state interaction of a conserved scalar $\eta/\rho r$. However, this form has numerous additional baroclinic vorticity generation terms, and offers no practical advantage over (A.1).

As in Part I, we separate each of the equations into terms acting on each of the three variables ψ_0, v_0, θ_0, and their temporal derivatives. Using the fact that the orders of time and spatial derivatives may be interchanged, the forced STHE can be reduced to three coupled equations that may be represented symbolically as the matrix system

$$\begin{bmatrix} B_{\psi\psi} & B_{\psi v} & B_{\psi\theta} \\ B_{v\psi} & B_{vv} & B_{v\theta} \\ B_{\theta\psi} & B_{\theta v} & B_{\theta\theta} \end{bmatrix} \begin{bmatrix} \dot{\psi}_0 \\ \dot{v}_0 \\ \dot{\theta}_0 \end{bmatrix} = \begin{bmatrix} A_{\psi\psi} & A_{\psi v} & A_{\psi\theta} \\ A_{v\psi} & A_{vv} & A_{v\theta} \\ A_{\theta\psi} & A_{\theta v} & A_{\theta\theta} \end{bmatrix} \begin{bmatrix} \psi_0 \\ v_0 \\ \theta_0 \end{bmatrix} + \begin{bmatrix} h_\psi \\ h_v \\ h_\theta \end{bmatrix}. \tag{A.3}$$

The elements of the two matrices each represent a sum of functions and operators that multiply (or operate on) each variable. The first subscript refers to the equation

[A1] The alternative streamfunction–velocity relationship (see footnote 1) results in a streamfunction operator with terms similar to those seen in a cylindrical coordinate Laplacian operator, but with an abundance of extra terms involving derivatives of the density.

with which the operators are associated, and the second subscript refers to the variable on which they operate. The time evolution operator $\mathbf{T} = \mathbf{B}^{-1}\mathbf{A}$.

The operator $A_{\psi\psi}$ consists of minus the second through sixth terms of the lhs, plus the friction terms on the rhs of (A.1), each modified so as to operate on ψ_0 (rather than u_0 or w_0) according to (2.6). For brevity, these are not repeated. The other terms of **A** and **B** are[A2]

$$A_{\psi v} = \frac{\partial}{\partial z}\overline{\rho}(2\overline{\Omega} + f), \tag{A.4}$$

$$A_{\psi\theta} = \frac{\partial}{\partial r}\overline{\rho}\frac{g}{\overline{\theta}}, \tag{A.5}$$

$$A_{v\psi} = \left(\frac{\partial \overline{v}}{\partial r} + \overline{\Omega} + f\right)\frac{1}{\overline{\rho} r}\frac{\partial}{\partial z} - \frac{\partial \overline{v}}{\partial z}\frac{1}{\overline{\rho} r}\frac{\partial}{\partial r}, \tag{A.6}$$

$$A_{vv} = -\overline{u}\frac{\partial}{\partial r} - \overline{w}\frac{\partial}{\partial z} - \frac{\overline{u}}{r} + F_v, \tag{A.7}$$

$$A_{v\theta} = 0, \tag{A.8}$$

$$A_{\theta\psi} = \frac{\partial \overline{\theta}}{\partial r}\frac{1}{\overline{\rho} r}\frac{\partial}{\partial z} - \frac{\partial \overline{\theta}}{\partial z}\frac{1}{\overline{\rho} r}\frac{\partial}{\partial r}, \tag{A.9}$$

$$A_{\theta v} = 0, \tag{A.10}$$

$$A_{\theta\theta} = -\overline{u}\frac{\partial}{\partial r} - \overline{w}\frac{\partial}{\partial z} + F_\theta, \tag{A.11}$$

$$B_{\psi\psi} = -\frac{1}{r}\frac{\partial^2}{\partial r^2} - \frac{1}{r}\frac{\partial^2}{\partial z^2} + \frac{1}{r^2}\frac{\partial}{\partial r}, \tag{A.12}$$

$$B_{\psi v} = 0, \tag{A.13}$$

$$B_{\psi\theta} = 0, \tag{A.14}$$

$$B_{v\psi} = 0, \tag{A.15}$$

$$B_{vv} = 1, \tag{A.16}$$

$$B_{v\theta} = 0, \tag{A.17}$$

$$B_{\theta\psi} = 0, \tag{A.18}$$

$$B_{\theta v} = 0, \quad \text{and} \tag{A.19}$$

$$B_{\theta\theta} = 1. \tag{A.20}$$

The elements of **h** are

$$h_\psi = \frac{\partial}{\partial z}\overline{\rho}E_u - \frac{\partial}{\partial r}\overline{\rho}E_w, \tag{A.21}$$

$$h_v = E_v, \quad \text{and} \tag{A.22}$$

$$h_\theta = E_\theta. \tag{A.23}$$

[A2] The general sign convention of the terms in **A** and **B** are reversed from appendix A in Part I. For simplicity, the expressions for the friction operators are written the same as the friction terms.

APPENDIX B

Boundary Conditions for the Symmetric and Asymmetric Equations

In both Part I and here, variables are stored on Arakawa-C-type staggered grids. Here, the grid is augmented to include the cell corners, where values of streamfunction ψ and azimuthal vorticity η reside. In general, the conditions were no-normal-flow and free-slip (no stress) at each boundary; that is,

$$w_n = 0, \quad \frac{\partial u_n}{\partial z} = 0, \quad \frac{\partial v_n}{\partial z} = 0, \quad \frac{\partial \theta_n}{\partial z} = 0 \quad \text{at } z = 0 \quad \text{and} \quad z = z_{\max}, \tag{B.1}$$

$$u_n = 0, \quad \frac{\partial w_n}{\partial r} = 0, \quad \frac{\partial v_n}{\partial r} = 0, \quad \frac{\partial \theta_n}{\partial r} = 0 \quad \text{at } r = r_{\max}, \tag{B.2}$$

$$u_n = 0, \quad v_n = 0, \quad w_n = 0, \quad \theta_n = 0 \quad \text{at } r = 0, \quad n > 1, \tag{B.3}$$

$$\frac{\partial u_n}{\partial r} = 0, \quad \frac{\partial v_n}{\partial r} = 0, \quad w_n = 0, \quad \theta_n = 0 \quad \text{at } r = 0, \quad n = 1, \tag{B.4}$$

$$u_n = 0, \quad v_n = 0, \quad \frac{\partial w_n}{\partial r} = 0, \quad \frac{\partial \theta_n}{\partial r} = 0 \quad \text{at } r = 0, \quad n = 0. \tag{B.5}$$

The last two sets are modified for the special cases of $n = 1$, which has flow across the center, and for axisymmetric flow.

In the asymmetric equations, v_n is not an independent variable so an additional condition must be added to u_n or w_n. For example, because,

$$v_n = \frac{ir}{n}\frac{1}{\overline{\rho}r}\frac{\partial}{\partial r}(\overline{\rho}ru_n) + \frac{ir}{n}\frac{1}{\overline{\rho}}\frac{\partial}{\partial z}(\overline{\rho}w_n) \qquad \text{(B.6)}$$

(see Part I, appendix A), then at $z = 0$:

$$0 = \frac{\partial v_n}{\partial z} = \frac{\partial}{\partial z}\left[\frac{ir}{n}\frac{1}{\overline{\rho}r}\frac{\partial}{\partial r}(\overline{\rho}ru_n) + \frac{ir}{n}\frac{1}{\overline{\rho}}\frac{\partial}{\partial z}(\overline{\rho}w_n)\right]. \qquad \text{(B.7)}$$

As the vertical density gradient terms are relatively small, and using $\partial u_n/\partial z = 0$, (B.7) is solved approximately by

$$\frac{\partial^2 w_n}{\partial z^2} = 0. \qquad \text{(B.8)}$$

Similarly, $1/r$ terms in (B.7) are neglected near the outer boundary. In general then, the free-slip condition on v_n at each boundary is enforced by adding the additional condition that the second derivative of the normal velocity is zero. As $r \to 0$, however, we have $v_n = iu_n/n$ automatically, and no additional boundary condition is needed.

For the symmetric equations, the no-normal-flow and free-slip velocity conditions on u and w are enforced by setting

$$\psi_0 = 0, \quad \frac{\partial^2\psi_0}{\partial z^2} = 0 \quad \text{at } z = 0 \quad \text{and} \quad z = z_{\max}, \qquad \text{(B.9)}$$

$$\psi_0 = 0, \quad \frac{\partial^2\psi_0}{\partial r^2} = 0 \quad \text{at } r = r_{\max}, \qquad \text{(B.10)}$$

$$\psi_0 = 0, \quad \psi_0 \sim r^2 \quad \text{at } r = 0. \qquad \text{(B.11)}$$

This last condition comes from applying $\partial w_0/\partial r = 0$ to (2.6) as $r \to 0$.

Numerically, boundary conditions are enforced on grid points at and adjacent to the domain boundaries, using locally third-order accurate Taylor series extrapolations of the interior data. For example, recall that u points are staggered relative to the upper and lower boundaries. To enforce $\partial u/\partial z = 0$ on $z = 0$, we set

$$0 = \left.\frac{\partial u}{\partial z}\right|_{z=2\Delta z} - 2\Delta z\left.\frac{\partial^2 u}{\partial z^2}\right|_{z=2\Delta z} + \frac{1}{2}(2\Delta z)^2\left.\frac{\partial^3 u}{\partial z^3}\right|_{z=2\Delta z}. \qquad \text{(B.12)}$$

Using second-order, centered difference schemes for each of these derivatives, we may solve for the first data point u_1 (at $z = \Delta z/2$) in terms of its neighbors,

$$u_1 = 2u_2 - \frac{4}{3}u_3 + \frac{1}{3}u_4. \qquad \text{(B.13)}$$

(Here, the subscripts refer to the grid point.) For normal velocities, such as w at $z = 0$, the data points are unstaggered and we have the two conditions $w = 0$ and $\partial^2 w/\partial z^2 = 0$ (these conditions apply to ψ as well). The first condition is easily enforced by setting $w_1 = 0$ (which sits on the boundary), and the second is found from a Taylor series expansion similar to (B.12). Using the first condition again, we find

$$w_2 = \frac{10}{9}w_3 - \frac{5}{9}w_4 + \frac{1}{9}w_5. \qquad \text{(B.14)}$$

Note that we have assumed Δz is constant. This is allowable because the stretching functions were designed to be constant near the boundaries (see Part I, appendix B).

REFERENCES

Black, M. L., J. F. Gamache, F. D. Marks Jr., C. E. Samsury, and H. E. Willoughby, 2002: Eastern Pacific Hurricanes Jimena of 1991 and Olivia of 1994: The effect of vertical shear on structure and intensity. *Mon. Wea. Rev.,* **130,** 2291–2312.

Braun, S. A., 2002: A cloud-resolving simulation of Hurricane Bob (1991): Storm structure and eyewall buoyancy. *Mon. Wea. Rev.,* **130,** 1573–1592.

Carr, L. E., and R. T. Williams, 1989: Barotropic vortex stability to perturbations from axisymmetry. *J. Atmos. Sci.,* **46,** 3177–3191.

Corbosiero, K. L., and J. Molinari, 2002: The effects of vertical wind shear on the distribution of convection in tropical cyclones. *Mon. Wea. Rev.,* **130,** 2110–2123.

Eastin, M. D., 2002: Observational analysis of bouyancy in intense hurricane eyewalls. Preprints, *25th Conf. on Hurricanes and Tropical Meteorology,* San Diego, CA, Amer. Meteor. Soc., 640–641.

Eliassan, A., 1951: Slow thermally or frictionally controlled meridional circulation in a circular vortex. *Astrophys. Norv.,* **5,** 19–60.

Enagonio, J., and M. T. Montgomery, 2001: Tropical cyclogenesis via convectively forced vortex Rossby waves in a shallow water primitive equation model. *J. Atmos. Sci.,* **58,** 685–706.

Feuer, S. E., J. F. Gamache, M. L. Black, and F. D. Marks Jr., 2002: A multiple aircraft experiment in Hurricane Humberto (2001). Part I: Wind fields. Preprints, *25th Conf. on Hurricanes and Tropical Meteorology,* San Diego, CA, Amer. Meteor. Soc., 206–207.

Frank, W. M., and E. A. Ritchie, 2001: Effects of vertical wind shear on the intensity and structure of numerically simulated hurricanes. *Mon. Wea. Rev.,* **129,** 2249–2269.

Hack, J. J., and W. H. Schubert, 1986: Nonlinear response of atmospheric vortices to heating by organized cumulus convection. *J. Atmos. Sci.,* **43,** 1559–1573.

Melander, M. V., J. C. McWilliams, and N. J. Zabusky, 1987: Axisymmetrization and vorticity-gradient intensification of an isolated two-dimensional vortex through filamentation. *J. Fluid Mech.,* **178,** 137–159.

Michalakes, J., S. Chen, J. Dudhia, L. Hart, J. Klemp, J. Middlecoff, and W. Skamarock, 2001: Design of a next generation weather research and forecast model. *Development in Tera-computing: Proceedings from the Ninth ECMWF Workshop on the Use of High Performance Computing in Meterology,* W. Zwieflhofer and N. Kreitz, Eds., World Scientific, 269–276.

Möller, J. D., and M. T. Montgomery, 1999: Vortex Rossby waves and hurricane intensification in a barotropic model. *J. Atmos. Sci.,* **56,** 1674–1687.

——, and ——, 2000: Tropical cyclone evolution via potential vorticity anomalies in a three-dimensional balance model. *J. Atmos. Sci.,* **57,** 3366–3387.

——, and L. J. Shapiro, 2002: Balanced contributions to the intensification of Opal as diagnosed from a GFDL model forecast. *Mon. Wea. Rev.,* **130,** 1866–1881.

Montgomery, M. T., and R. J. Kallenbach, 1997: A theory for vortex Rossby waves and its application to spiral bands and intensity

changes in hurricanes. *Quart. J. Roy. Meteor. Soc.*, **123,** 435–465.
——, and J. Enagonio, 1998: Tropical cyclogensis via convectively forced vortex Rossby waves in a three-dimensional quasi-geostrophic model. *J. Atmos. Sci.*, **55,** 3176–3207.
Nolan, D. S., 2001: The stabilizing effects of axial stretching on turbulent vortex dynamics. *Phys. Fluids*, **13,** 1724–1738.
——, and B. F. Farrell, 1999a: Generalized stability analyses of asymmetric disturbances in one- and two-celled vortices maintained by radial inflow. *J. Atmos. Sci.*, **56,** 1282–1307.
——, and ——, 1999b: The intensification of two-dimensional swirling flows by stochastic asymmetric forcing. *J. Atmos. Sci.*, **56,** 3937–3962.
——, and M. T. Montgomery, 2002a: Three-dimensional stability analyses of tornado-like vortices with secondary circulations. Preprints, *21st Conf. on Severe Local Storms*, San Antonio, TX, Amer. Meteor. Soc., 477–480.
——, and ——, 2002b: Nonhydrostatic, three-dimensional perturbations to balanced, hurricane-like vortices. Part I: Linearized formulation, stability, and evolution. *J. Atmos. Sci.*, **59,** 2989–3020.
Persing, J., M. T. Montgomery, and R. T. Tuleya, 2002: An illustration of hurricane–trough interaction in the GFDL model. *Mon. Wea. Rev.*, **130,** 298–317.
Reasor, P. D., M. T. Montgomery, F. D. Marks Jr., and J. F. Gamache, 2000: Low-wavenumber structure and evolution of the hurricane inner core observed by airborne dual-Doppler radar. *Mon. Wea. Rev.*, **128,** 1653–1680.
Schubert, W. H., and J. J. Hack, 1982: Inertial stability and tropical cyclone development. *J. Atmos. Sci.*, **39,** 1687–1697.
Shapiro, L. J., 2000: Potential vorticity asymmetries and tropical cyclone evolution in a moist three-layer model. *J. Atmos. Sci.*, **57,** 3645–3662.
——, and H. E. Willoughby, 1982: The response of balanced hurricanes to local sources of heat and momentum. *J. Atmos. Sci.*, **39,** 378–394.
Smith, G. B., II, and M. T. Montgomery, 1995: Vortex axisymmetrization: Dependence on azimuthal wavenumber or asymmetric radial structure changes. *Quart. J. Roy. Meteor. Soc.*, **121,** 1615–1650.
Takemi, T., and R. Rotunno, 2003: The effects of subgrid model mixing and numerical filtering in simulations of mesoscale cloud systems. *Mon. Wea. Rev.*, **131,** 2085–2101.
Wang, Y., 2002: Vortex Rossby waves in a numerically simulated tropical cyclone. Part I: Overall structure, potential vorticity, and kinetic energy budgets. *J. Atmos. Sci.*, **59,** 1213–1238.
Weisman, M. L., W. C. Skamarock, and J. B. Klemp, 1997: The resolution dependence of explicitly modeled convective systems. *Mon. Wea. Rev.*, **125,** 527–548.
Wicker, L. J., and W. C. Skamarock, 2002: Time-splitting methods for elastic models using forward time schemes. *Mon. Wea. Rev.*, **130,** 2088–2097.
Yang, S., W. S. Olson, C. D. Kummerow, S. Chen, Z. Haddad, and E. Smith, 2002: Latent heating structure of hurricanes from TRMM measurements. Preprints, *25th Conf. on Hurricanes and Tropical Meteorology*, San Diego, CA, Amer. Meteor. Soc., 511–512.
Zhang, D.-L., Y. Liu, and M. K. Yau, 2002: A multiscale numerical study of Hurricane Andrew (1992). Part V: Inner-core thermodynamics. *Mon. Wea. Rev.*, **130,** 2745–2763.